ELSEVIER

Contents lists available at ScienceDirect

# Geochimica et Cosmochimica Acta

journal homepage: www.elsevier.com/locate/gca





# Molybdenum in basalt-hosted seafloor hydrothermal systems: Experimental, theoretical, and field sampling approaches

Guy N. Evans a,\*, Laurence A. Coogan b, Betül Kaçar c, William E. Seyfried a

- Department of Barth and Environmental Sciences, University of Minnesota, Minneapolis, MN 55455, USA
- b School of Earth and Ocean Sciences, University of Victoria, Victoria, British Columbia, Canada
- <sup>c</sup> Department of Bacteriology, University of Wisconsin Madison, Madison, WI 53706, USA

#### ARTICLE INFO

Associate editor: Eva Stüeken

Keywords: Barly life Transition metals Micronutrient NASA MUSE Consortia Ocean Networks Canada

#### ABSTRACT

Seafloor hydrothermal vents represent potential sources of Mo and other biologically relevant transition metals to the global ocean, complementing continental runoff. Here, we use a combination of experimental, theoretical, and field-sampling approaches to investigate the behavior of Mo in basalt-hosted seafloor hydrothermal systems to provide insight into the processes controlling Mo concentrations in hydrothermal fluids and to derive estimates of vent fluid Mo concentrations and fluxes. Results of this study demonstrate that reaction fluids generated from 350 °C, 500 bar hydrothermal basalt alteration experiments contain 775–801 nmol/kg Mo and are thus comparable to a recently collected time series of natural seafloor vent fluids that contained 200–220 nmol/kg Mo at 302 °C and 29–30 nmol/kg at 281–282 °C (Evans et al., 2023). Synchrotron-based analyses of experimentally altered basalt produced in this study and additional natural samples of altered oceanic crust originally collected from Pito Deep Rift reveal the presence of Mo-rich particles consistent with trace molybdenite. Comparisons of Mo:Cu ratios in natural vent fluids and near-vent sediment trap samples from Main Endeavour Field indicate that vent fluid Mo is readily incorporated into buoyant plume particles and advected out of the near-vent field, analogous to previous mass balance studies of Cu in this region.

Thermodynamic calculations of molybdenite solubility in the context of mineral-buffered hydrothermal fluids and comparisons with natural and experimental hydrothermal fluids suggest that high-temperature vent fluids contain 30–1500 nmol/kg Mo. While a minor component of the modern Mo budget, hydrothermal Mo fluxes are estimated to have constituted  $0.3-200\times$  the contemporaneous continental weathering fluxes prior to the  $\sim 2.4$  Ga ago "Great Oxidation Event" and widespread oxidative continental weathering. Overall, identification of hydrothermal vents as a source of Mo-rich plume particles with potential for dispersal into the wider marine environment has significant implications for hypotheses regarding the co-evolution of Life and Earth's environments, specifically the form and availability of Mo in anoxic Archean-Eon oceans, where Mo-dependent enzymatic pathways are thought to have emerged and subsequently evolved.

#### 1. Introduction

Nutrient transition metals are key components of biological enzymes and the emergent metabolic pathways that sustain Life and drive Barth's biogeochemical cycles (e.g., Morel and Price, 2003; Falkowski et al., 2008). Illustrative of the vital role of transition metals in biology, Mo enables biological uptake of molecular nitrogen though its functional role in nitrogenase (Burgess and Lowe, 1996). Additional Mo-containing enzymes are active in biological carbon, sulfur, and nitrogen cycling, wherein W may sometimes act as a functional replacement (Maia et al., 2016). Molybdenum-free nitrogenase variants containing V or reduced

Fe only have also been identified (Joerger et al., 1988; Miller and Eady, 1988). The foundational role of Mo and other nutrient transition metals in biologic- and, potentially, prebiotic chemistry underscores the need for a better understanding of the controls on transition metal availability in various natural systems and ecologically relevant environments throughout geological time.

Current environmental cycling of Mo is characterized by the vulnerability of geologically exposed Mo-containing sulfide minerals to oxidative weathering and the high solubility of molybdate (MoO4<sup>+</sup>) in oxidized aqueous fluids (Miller et al., 2011; Kendall et al., 2017; Greaney et al., 2018). However, experimental weathering and isotopic mass

E-mail address: gevans@umn.edu (G.N. Evans).

<sup>\*</sup> Corresponding author.

balance studies (Johnson et al., 2019, Johnson et al., 2021) indicate that these weathering fluxes would have been much reduced prior to widespread oxidation of Earth's continental surface environments—the commonly referenced Great Oxidation Event (GOE) ~2.4 Ga ago (Holland, 2002; Canfield, 2005; Lyons et al., 2014)—when Modependent nitrogenase (Stüeken et al., 2015; Garcia et al., 2020; Parsons et al., 2021) and other Mo-dependent enzymes (Schoepp-Cothenet et al., 2012; Weiss et al., 2016) are thought to have evolved. Consequently, it has been proposed that life was Mo- (and V-) limited prior to the GOE (e.g., Anbar and Knoll, 2002; Zerkle et al., 2006; Sanchez-Baracaldo et al., 2014), consistent with geochemical and Mo-isotope evidence from Archean Eon marine sedimentary rocks (Wille et al., 2013) indicating that seawater was Mo-poor compared to modern, oxygenated oceans.

In this context, it has been proposed that V- and Fe-only nitrogenases represent more primitive variants that evolved under low-Mo conditions characteristic of pre-GOE oceans (Anbar and Knoll, 2002). However, more in-depth genetic and phylogenetic investigations indicate that Modependent nitrogenase is, in fact, ancestral to these metal-replaced alternatives (Raymond et al., 2004; Boyd et al., 2011; Garcia et al., 2020, 2022). Further complicating this picture are demonstrations that Mo concentrations in modern anoxic aqueous environments are rarely, if ever, depleted to levels ( 5 nmol/kg; Zerkle et al., 2006) thought to be limiting for nitrogen fixation (Helz, 2021) and that mineral-bound forms of Mo, V, and Fe are sufficiently bioavailable for nitrogen fixation (Sheng et al., 2023). Because of these various complications, a better understanding of the quantities and forms of Mo and other transition metal inputs to the Archean Eon ocean is necessary to adequately characterize the environments in which these metal-dependent metabolisms may have emerged and subsequently evolved.

Seafloor hydrothermal vents are an important source of transition metals to the deep ocean and may represent an important source of Mo to the pre-GOE ocean characterized by lower Mo inputs from continental runoff, Mo-poor seawater compositions, and estimated greater hydrothermal activity (e.g., Kamber, 2010). However, modern hydrothermal Mo fluxes are poorly constrained, having been overlooked in the context of much larger continental weathering fluxes (Miller et al., 2011; Kendall et al., 2017), obscured by high modern seawater concentrations (108 5 nmol/kg, Ho et al., 2018), and suffering from a lack of analytical attention to vent-fluid sampler precipitate fractions (so-called dregs) into which Mo preferentially partitions (Trefry et al., 1994; Schmidt et al., 2007; Evans et al., 2023). The processes by which Mo may enter and be transported within seafloor hydrothermal systems are likewise poorly constrained.

Here, we examine processes controlling Mo concentrations in seafloor hydrothermal vent fluids through a series of 350 °C, 500 bar hydrothermal basalt alteration experiments, thermodynamic models of Mo speciation and mineral saturation, and comparisons of experimental reaction fluids and reacted solids with natural samples of seafloor hydrothermal vent fluids, near-field sediment trap particles, and hydrothermally altered oceanic crust. We additionally evaluate the extent to which these processes may impact understandings of hydrothermal Mo sources to modern oxygenated and ancient anoxic ocean environments. Data for V, W and other nutrient transition metals are also reported.

## 2. Methods

## 2.1. Hydrothermal experiments

## 2.1.1. Experimental design

Hydrothermal basalt alteration experiments were conducted at the University of Minnesota in a  $\sim$ 70 ml titanium-capped gold reaction cell (Seyfried et al., 1987) loaded into a Kuentzel-closure 316 stainless-steel pressure vessel (Parker Autoclave Engineers, Erie, PA, USA). Pressure was maintained at 500 1 bar by water-line connection to a Teledyne 260D ISCO syringe pump (Teledyne ISCO, Lincoln NE, USA) calibrated

against a 750-bar pressure gauge (Heise, Stratford, CT, USA). Temperature was maintained at 350 5 C by a custom-built resistance coil furnace linked to a proportional-integral-derivative temperature controller (Watlow, Winona, MN, USA) controlled and monitored through a type-K thermocouple (Omega Engineering, Norwalk, CT, USA) calibrated using a Hot Point Dry Bock calibrator (Omega Engineering, Norwalk, CT, USA).

Solid reactants are 40.00 g No. 100 No. 35 sieve-size (150 500 m diameter) crushed seafloor basalt originally collected from the East Pacific Rise (EPR) (Cruise AT-37, Alvin Dive 4838, 09 50.13 N, 104 17.353 W). This sample is an aphanitic enriched mid-ocean ridge basalt containing plagioclase (labradorite), pyroxene (augite), and minor titanium-bearing magnetite. A more detailed petrologic description of this sample may be found in Perfit et al. (2003).

Fluid reactants are alternately a (Na, K) Cl solution initially containing Na 540 mmol/kg, K 10 mmol/kg, and Cl 550 mmol/kg and a (Na, Ca) Cl solution initially containing Na 400 mmol/kg, Ca 45 mmol/kg, and Cl 490 mmol/kg. The fluid:rock mass ratio was initially 1:1 but necessarily decreased as fluid samples were withdrawn, to a minimum of 0.76 at final sampling (see Results, Table 3). Experiments were run for 50 55 days, guided by previous hydrothermal basalt alteration experiments demonstrating near steady-state metal concentrations after  $\sim$ 30 days of reaction at 350 C (Seewald and Seyfried, 1990).

## 2.1.2. Sample collection

Fluid samples were collected from the gold cell reaction vessel through a titanium exit tube (outer diameter 1/4-inch (6.4 mm), inner diameter 1/16-inch (1.6 mm)) after flushing with  $\sim 1 \text{ ml}$  reaction fluid to clear the exit tube of any materials deposited between samplings. Sample aliquots intended for metals analyses were collected using a separate gas-tight quick-quench Ti piston sampler that allowed for rapid extraction of experimental fluid samples (Xing et al., 2022). Use of quick-quench samplers is intended to prevent deposition of temperature sensitive metals such as Mo and Cu in the sampling line. Metals samples were divided into a dissolved fraction obtained by pipetting fluid out of the piston sampler following sample cooling and depressurization and a precipitate fraction obtained by rinsing the sampler volume and titanium tubing with 1 M HCl prepared from trace metal grade 12 N HCl (Fisher Scientific, Pittsburgh, PA, USA) and 18.2 M cm <sup>1</sup> deionized water. The dissolved fraction was acidified to pH 1 by addition of 1 M HCl, likewise prepared. Residual post-reaction solid materials were collected at the end of the experiment, rinsed with 18.2 M cm  $^{1}$  deionized water, dried initially in Ar at  $\sim$ 25 C and then dried more completely in air at 40 C. In preparation for elemental analyses, fluid samples were diluted ~100 in a 2% HNO<sub>3</sub> matrix prepared from trace metal grade 70% HNO3 (Fisher Scientific, Pittsburgh, PA, USA) and 18.2 M cm <sup>1</sup> deionized water. Rock samples were digested using microwave assisted aqua regia HF digestion followed by boric acid HF neutralization (MARS 5, CEM Corp., Matthews, NC, USA) and diluted in 2% trace metal grade  $HNO_3$  to a total dilution factor of ~15,000 for trace elements and ~10 million for major elements.

# 2.2. Geochemical analyses

## 2.2.1. Fluid chemistry

Geochemical analyses of pre- and post-reaction fluids and solids were conducted at the University of Minnesota. Experimental reaction fluids were analyzed for pH by ROSS pH electrode (Thermo Fisher Scientific, Waltham, MA, USA), total dissolved sulfide by iodometric titration (U.S. EPA, Method 9034),  $\rm H_2$  by gas chromatography (Agilent 6980, Santa Clara, CA, USA), and major anions by ion chromatography (Dionex ICS-5000, Thermo Fisher Scientific, Waltham, MA, USA). Analytical details are provided in Supplementary Materials.

#### 2.2.2. Elemental analyses

Elemental analyses of reaction fluid and rock samples were conducted using a triple quadrupole inductively coupled plasma mass spectrometer (TQ-ICP-MS) (iCAP-TQ, Thermo Fisher Scientific iCAP TQ, Waltham, MA, USA). Elemental analyses were calibrated using matrix-matched calibration lines prepared from NIST-traceable single- and multi-element standards (SPEX CertiPrep, Metuchen, NJ, USA) and Sc, Y, Ir in-line internal standards. Data quality is evaluated by recovery of gravimetrically prepared matrix-matched check samples for fluids and concurrent analyses of USGS standard reference material BHVO-1 for rocks. Fluid metal concentrations were reconstructed by mathematical addition of "dissolved" and "precipitate" fractions.

#### 2.2.3. Electron microprobe analysis

Selected aliquots of unreacted and reacted basalt were mounted in epoxy and prepared as 30-µm thin sections. Electron microprobe analyses (EMPA) of major and minor elements (Si, Al, Ca, Fe, Mg, Na, Ti, Mn, K, Cr) were performed at the University of Minnesota using a JXA-8530FPLus Electron Probe (JEOL, Tokyo, Japan). Analysis spot size was 3 µm; beam energy was 15 kV; count times ranged between 10 and 20 s; spectra were collected on TAP, PETL, TAPL, and LIFL crystals. Calibration is based on a set of in-house silicate and oxide standards. Back-scatter electron images were also collected.

#### 2.3. Natural samples

To better contextualize results from hydrothermal experiments and to provide greater insight into the behavior of natural systems, experimentally derived fluid and solid samples are compared to natural samples of seafloor hydrothermal fluids, particles collected in near-field sediment traps, and hydrothermally altered oceanic crust. Seafloor hydrothermal fluids are represented by published analyses and a recent time series of nine 281–304 °C vent fluid samples collected from the Main Endeavour Field (MEF) (47° 57′ N, 129° 06′ W, ~2200 m water depth) from October 2019 to May 2020 (Seyfried et al., 2022; Evans et al., 2023). As evidenced by low Mg concentrations, these vent fluid samples exhibit little-to-no contamination by surrounding seawater (Seyfried et al., 2022) and contain 29–220 nmol/kg Mo (Evans et al., 2023), a range which spans modern seawater (Mo = 108 ± 5 nmol/kg, Ho et al., 2018). Sediment trap samples from roughly the same region of MEF were collected in 2014–2015 (Fig. 1; Coogan et al., 2017).

The behavior of Mo in the subsurface is examined by reference to samples collected from Pito Deep Rift (Fig. 2A), a tectonic window that exposes ~3 Ma altered oceanic crust originally formed at the southern Bast Pacific Rise. Several samples contain elevated Mo concentrations up to 9.26 µg/g Mo (Fig. 2B; Zhu, 2016). One of these Mo-enriched samples, 022205-0852 (22°55.44′8, 111°52.8′W, 3197 mbsl, Heft et al., 2008), was selected for synchrotron-based analysis. The selected sample is a plagioclase-phyric normal mid-ocean ridge basalt containing secondary

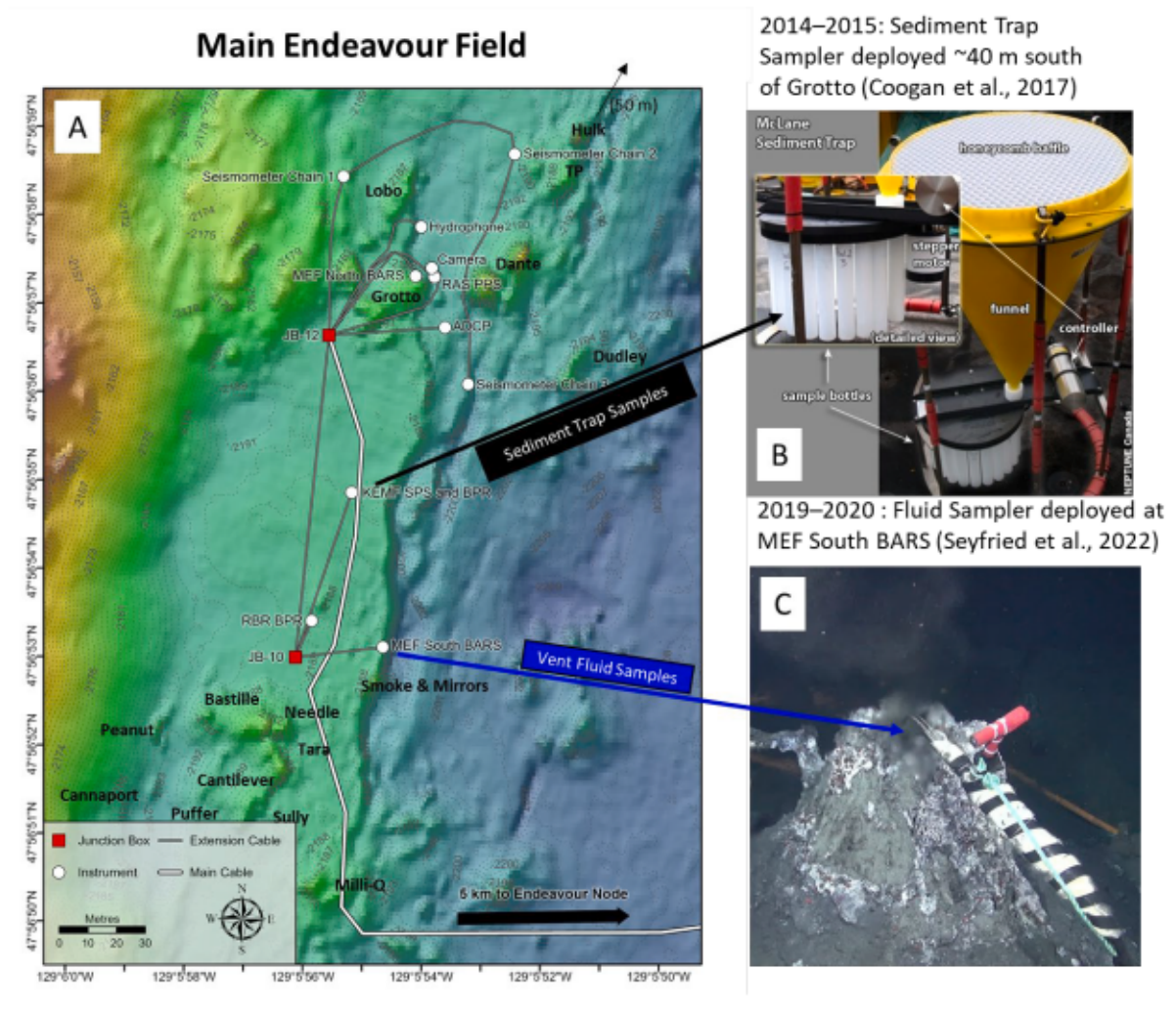


Fig. 1. (A) Labeled bathymetric map of Main Endeavour Field showing historical vent/deposit structure names (Delaney et al., 1992) and infrastructure of Ocean Network Canada's NEPTUNE cabled observatory (Kelley et al., 2014) as well as the locations of (B) sediment trap samples collected in 2014–2015, ~40 m south of the Grotto vent deposit (Coogan et al., 2017) and (C) vent fluid time series collected in 2019–2020 (Seyfried et al., 2022).

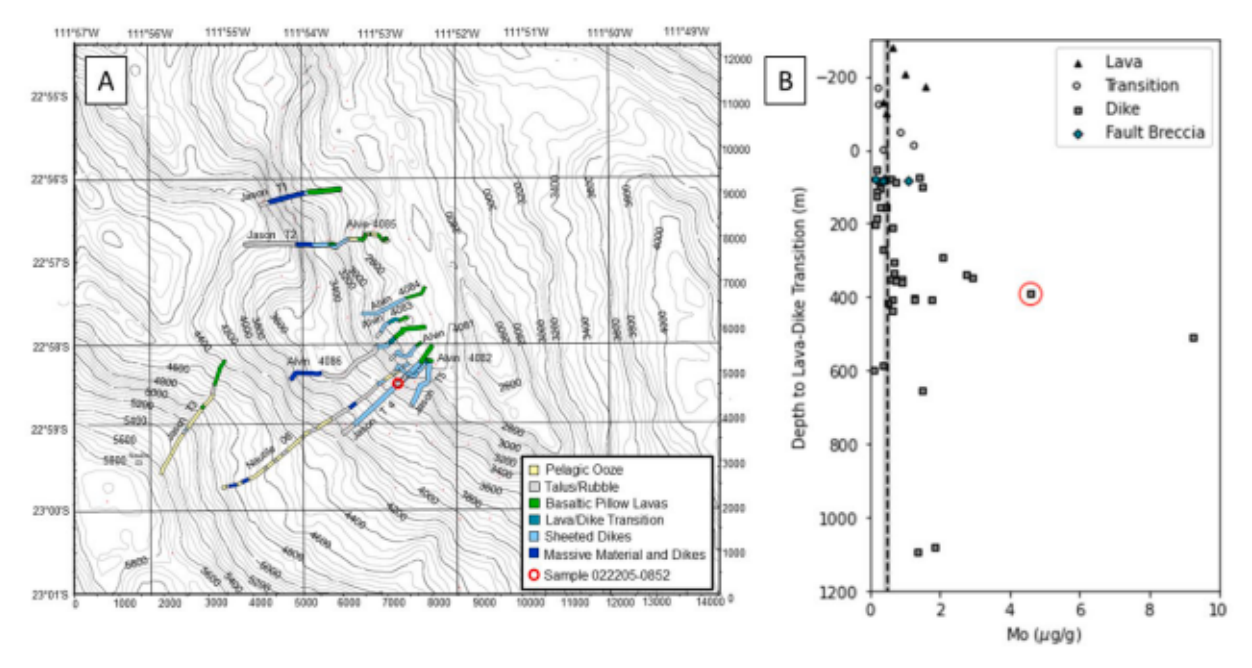


Fig. 2. (A) Summary submersible investigations of Pito Deep Rift, Area B: Jason II Transects, Alvin Dives from Pito Deep Cruise AT11-23 in 2005 and Nautile dives (from Hekinian et al., 1993). Approximate location of sample 022205-0852 shown by red circle. Figure modified from original by Jeff Karson. (B) Molybdenum concentrations in hydrothermally altered oceanic crust from Pito Deep Rift plotted against approximate stratigraphic depth relative to the lava-dike transition zone. The lava-dike transition is identified as the deepest observation of a lava for each submersible transect; original water depth is 2600-4200 m below sea level (Heft et al., 2008). Sample 022205-0852 selected for synchrotron analysis, which contains  $4.6 \,\mu$ g/g Mo (Zhu, 2016), is highlighted with a red circle. The dashed black line and gray bar indicate the estimated fresh-rock Mo concentrations of  $0.5 \pm 0.1 \,\mu$ g/g based on Yb concentrations in hydrothermally altered samples and covariation of Yb and Mo in fresh mid-ocean ridge basalt glasses (Zhu, 2016). Samples were originally selected for a study focused on subsurface metal enrichments and may therefore be biased toward Mo-enriched samples. (For interpretation of the references to color in this figure legend, the reader is referred to the web version of this article.)

plagioclase, amphibole, chlorite, and rare epidote collected from the sheeted dike section, 392 m below the lava-dike transition, (Heft et al., 2008). It contains 4.6 µg/g Mo (Zhu, 2016).

#### 2.4. Synchrotron-based analyses

Samples of pre- and post-reacted EPR basalt were prepared for synchrotron-based analyses at the Advanced Photon Source, Argonne National Laboratory, Argonne, IL, USA, beamline 13-ID-E, using a Si (1,1,1) double crystal monochromator and a Canberra SXD-7 16element Ge (3,3,1) detector. Incoming beam energy for micro-X-ray fluorescence (μ-XRF) maps was 20 keV. Data were processed using the Larch analysis package (Newville, 2013).

Spectra for Mo k-edge X-ray absorbance near-edge structure (Mo-XANES) analyses were collected in the pre-edge (19.900-19.990 keV; 2.5 eV resolution), near-edge (19.990-20.025 keV; 0.25 eV resolution), and EXAFS (2.562-8.000 A<sup>-1</sup>; 0.1 A<sup>-1</sup> resolution) regions of the Mo k-edge adsorption peak. Energy calibration was performed by assigning the maximum white line of Mo-foil analyzed in the same session to 20.000 keV, resulting in a E<sub>0</sub> shift of +2.998 eV. Standards include natural molybdenite (VWR, Radnor, PA, USA) and synthetic (NH<sub>4</sub>)<sub>2</sub>MoO<sub>4</sub>, (NH<sub>4</sub>)<sub>2</sub>MoS<sub>4</sub>, MoO<sub>2</sub>, and MoO<sub>3</sub> (Fisher Scientific, Pittsburgh, PA, USA). For µ-XRF maps, interferences on the Mo ka channel (17.030-17.710 keV) by Zr kb1 fluorescence at 17.6682 keV were corrected by reference to the Zr ka channel (15.510-16.030 keV).

## 2.5. Thermodynamic modeling

Thermodynamic modeling was performed using Geochemists' Workbench (GWB) (Bethke and Yeakel, 2012) and a 500-bar thermodynamic database generated by PyGeochemCale (Awolayo and Tutolo, 2022). Thermodynamic data for aqueous species generally follow the Helgeson-Kirkham-Flowers (HKF) equation of state model (Tanger and

Helgeson, 1988; Shock and Helgeson, 1988; Shock et al., 1989; Shock and Helgeson, 1990). Thermodynamic data for Mo species were calculated using the Unitherm module of HCh (Shvarov, 2008) based on data from Robie and Hemingway (1995) for molybdenite, Shock et al. (1997) for MoO<sub>4</sub><sup>2</sup>, Minubayeva and Seward (2010) for HMoO<sub>4</sub> and H<sub>2</sub>MoO<sub>4</sub>(aq), and Shang et al. (2020) for NaHMoO<sub>4</sub>. In keeping with the most common practice for deriving thermodynamic properties of aqueous species from experimental data, neutral species are assigned unit activity coefficients. Relevant databases, input and output files are included in Supplementary Materials.

#### 3. Results

## 3.1. Composition of East Pacific Rise Basalt

Bulk geochemical analyses of EPR basalt (BEPR) are presented in Table 1; major and minor element compositions of constituent mineral phases are presented in Table 2. Solid phases include plagioclase with an average composition of Na<sub>0.35</sub>Ca<sub>0.65</sub>Al<sub>1.65</sub>Si<sub>2.35</sub>O<sub>8</sub>, pyroxene with an average composition of Ca<sub>0.34</sub>Mg<sub>0.47</sub>Fe<sub>0.19</sub>SiO<sub>3</sub>, an interstitial quenched melt phase exhibiting quench textures of bimodal Mg-rich and Mg-poor compositions, and minor titanium-bearing magnetite containing 11–12 wt% Ti and 0.4–0.5 wt% Mn (Table 2). Compared to surrounding minerals, quenched melt is enriched in incompatible elements, Na and K, and preferentially reacts during hydrothermal alteration (Fig. 3).

The initial BEPR sample contains  $3.3 \pm 0.1 \,\mu\text{g/g}$  Mo, which is substantially higher than the average mid-ocean ridge basalt (MORB) composition of Mo =  $0.46 \pm 0.05 \,\mu\text{g/g}$  and the enriched MORB composition of Mo =  $0.8 \pm 0.2 \,\mu\text{g/g}$  (Gale et al., 2013). Subsequent tests indicate that Mo enrichment in BEPR is not the result of laboratory contamination (Supplementary Materials) and perhaps reflect interactions with Mo-rich seawater during and after eruption at the seafloor (Perfit et al., 2003). While higher than expected, we emphasize

Table 1

Elemental analyses of East Pacific Rise basalt (BEPR) and USGS Standard Reference Material (BHVO-1) analyzed by inductively coupled plasma mass spectrometry (ICP-MS) at the University of Minnesota compared with published values for BHVO-1 from Jochum et al. (2016). BHVO-1 error is calculated as the concentration-normalized difference between ICP-MS analyses and published values for BHVO-1. 1 is one standard deviation uncertainty based on ICP-MS count rates.

		BEPR ICP-MS		BHVO-1 ICP-MS		BHVO-1 published		BHVO-1 Error
Unit	Average	1	Average	1	Average	1		
Major Eleme	ents							
$SiO_2$	wt %	48.9	0.3	49.4	4.4	49.8	0.12	1%
$Al_2O_3$	wt %	14.3	0.7	14.0	0.2	13.7	0.05	2%
CaO	wt %	12.1	0.2	10.9	0.4	11.4	0.04	4%
Fe <sub>2</sub> O <sub>3 (T)</sub>	wt %	11.4	0.5	13.0	0.1	12.3	0.04	6%
MgO	wt %	7.9	0.3	7.5	0.1	7.2	0.032	4%
Na <sub>2</sub> O	wt %	3.53	0.25	2.28	0.03	2.31	0.022	1%
TiO <sub>2</sub>	wt %	1.37	0.02	2.81	0.05	2.74	0.012	2%
MnO	wt %	0.17	0.01	0.17	0.00	0.17	0.0011	1%
K <sub>2</sub> O	wt %	0.14	0.02	0.49	0.04	0.53	0.0046	7%
Total	wt %	99.8		100.7		100.2		
Trace Transi	ition Metals							
V	g/g	308	4	278	19	314	3	12%
Cr	g/g	332	4	314	5	288	4	9%
Co	g/g	55	1	46	1	45	0	3%
Ni	g/g	96	1	118	1	120	2	2%
Cu	g/g	109	2	160	2	137	2	16%
Zn	g/g	101	2	157	3	105	2	49%
Mo	g/g	3.3	0.1	1.0	0.1	1.1	0.1	9%
Cd	ng/g	432	16	269	16	107	13	151%
W	ng/g	328	14	104	9	212	12	51%
Trace Alkali	Metals							
Li	g/g	4.3	0.52	4.68	0.48	4.68	0.09	0%
Rb	g/g	2.01	0.05	9.80	0.07	9.52	0.1	3%
Cs	ng/g	19	3	93	5	103	3	10%

Table 2

Electron microprobe analyses of solid phases in East Pacific Rise Basalt. Compositions of quenched melt phases exhibit variable compositions that generally correlate with MgO content. Representative compositions interpolated to 8 wt% and 1 wt% MgO are tabulated. Magnetite compositions are based on electron microprobe spot analyses centered on magnetite grains, extrapolated to SiO<sub>2</sub> 0 wt%. LOD Limit of Detection.

	LOD	Plagioclase		Pyroxene		Quenched Melt		Magnetite
	wt %	Average	1	Average	1	MgO 8 wt%	MgO 1 wt%	SiO <sub>2</sub> 0
SiO <sub>2</sub>	0.02	50.2	1.3	46.9	1.1	50.5	54.7	0.0
$Al_2O_3$	0.02	29.5	0.9	5.5	1.1	15.0	23.4	2.6
CaO	0.01	13.4	0.7	17.1	1.60	13.4	9.0	0
FeO	0.03	1.0	0.2	11.7	2.96	7.0	2.8	74.3
MgO	0.01	0.3	0.0	14.5	2.0	8.0	1.0	0
Na <sub>2</sub> O	0.01	3.94	0.42	0.33	0.1	2.9	5.9	0
$TiO_2$	0.01	0.08	0.03	1.61	0.34	0.90	0.3	18.23
MnO	0.03	0.01	0.01	0.27	0.08	0.16	0.0	0.56
$K_2O$	0.01	0.06	0.02	0.01	0.0	0.1	0.4	0
Total		98.6		97.9		97.9	97.5	95.7

that BEPR Mo concentrations are naturally occurring and not sufficiently anomalous to alter our interpretations.

Electron microprobe analyses of pre- and post-reaction BEPR samples indicate that the chemical compositions of mineral grain interiors change little during hydrothermal reaction. However, reacted surfaces and fine-grained secondary phases are evident in backscatter electron microscopy images (Fig. 3). Unfortunately, these secondary phases could not be directly analyzed by EMPA owing to small grain sizes and related difficulty in achieving a sufficient polished surface area.

# 3.2. Experimental fluid chemistry

Measured pH, H<sub>2</sub>, H<sub>2</sub>S, and SiO<sub>2</sub> of reaction fluids obtained from hydrothermal basalt alteration experiments (Table 3) are generally consistent with those of reversible hydrothermal basalt alteration experiments (e.g., Seyfried and Janecky, 1985; Seewald and Seyfried,

1990) indicating achievement of a quasi-equilibrium rock-buffered steady state condition. Compared to initial fluids, reaction fluids exhibit lower pH and elevated H<sub>2</sub>S, H<sub>2</sub>, Si, Al, and transition metal concentrations. Basalt reaction with a (Na, K) Cl fluid at 350 C, 500 bar leads to a 32.9 mmol/kg decrease in Na approximately balanced by a 23.9 mmol/kg increase in K, and a 4.5 mmol/kg increase in Ca (Table 3). Reaction with a (Na,Ca) Cl fluid leads to a 29.6 30.1 mmol/kg decrease in fluid Ca approximately balanced by a 25.7 mmol/kg increase in K and a 36 mmol/kg increase in Na (Table 3). Fluid pH is lower than that obtained from reaction with the (Na, K) Cl fluid, consistent with expectations based on the plagioclase (anorthite) epidote (clinozoisite) pH buffering reaction of Berndt et al., (1989):

Magnesium concentrations are 0.01~0.03~mmol/kg, which agrees well with results obtained from previous basalt alteration experiments

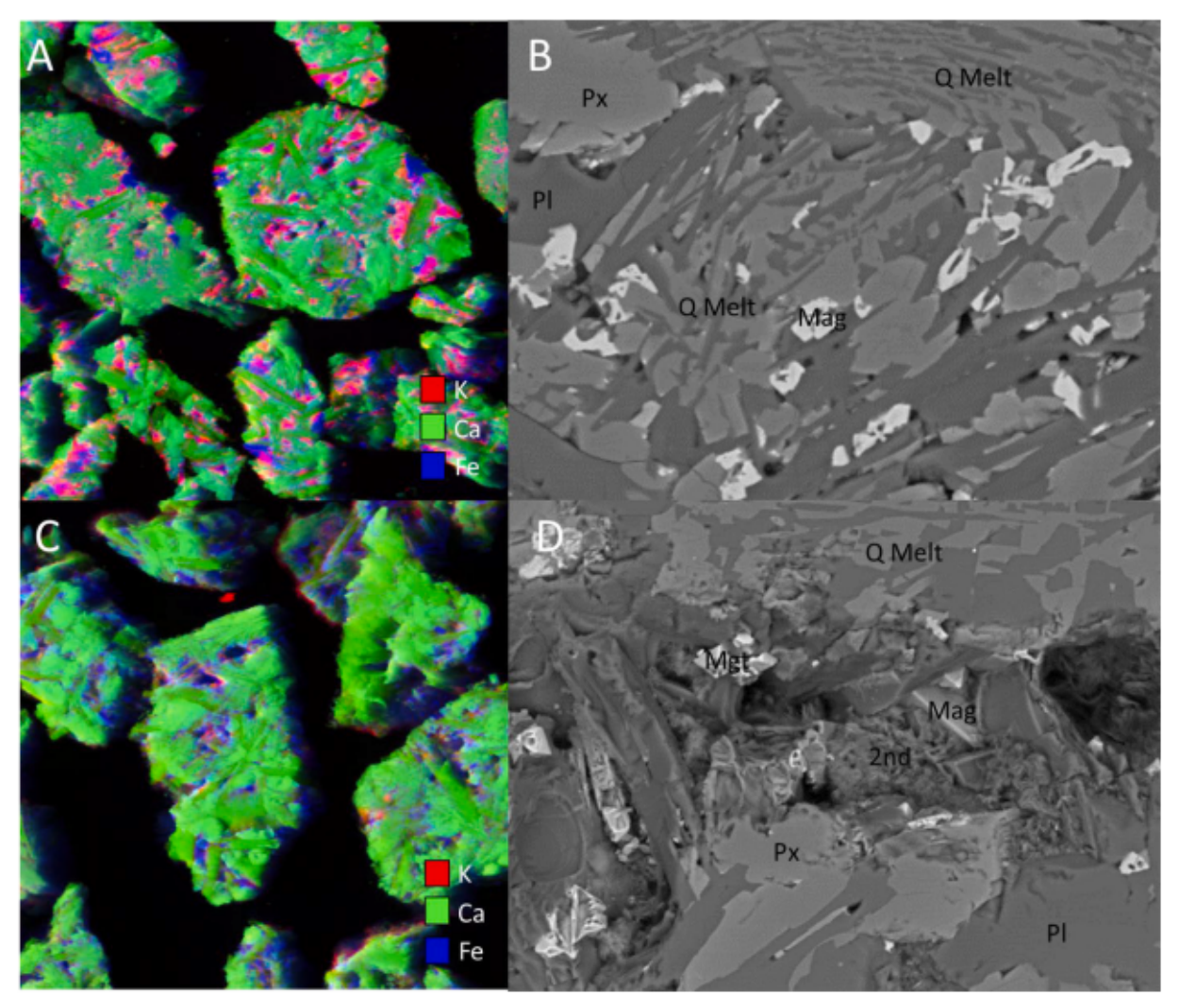


Fig. 3. Comparison of micro X-ray fluorescence (μ-XRF) maps and backscatter electron images of unaltered basalt (A and B) and basalt reacted with (Na,Ca) Cl solution at 350 °C (C and D) shows removal/reaction of K-rich quench melt phase (compare A and C) and presence of fine-grained secondary minerals (2nd) in reacted samples (D). The identity of secondary minerals is uncertain, but most likely chlorite based on morphological and optical characteristics. Image width of μ-XRF maps is 1 mm; color scheme is K (red), Ca (green), Fe (blue); plagioclase appears as bright green, pyroxene as dull green, magnetite as blue, and quenched melt as red/magenta; incoming beam energy is 7 keV. Image width of backscattered electron images is 100 μm. Pl = plagioclase; Px = pyroxene; Q Melt = quenched melt; Mag = magnetite; 2nd = secondary minerals. (For interpretation of the references to color in this figure legend, the reader is referred to the web version of this article.)

involving Mg-free (NaCl solution) and Mg-containing (i.e., artificial seawater) starting fluids. (Seyfried and Bischoff, 1981).

Trace transition metal concentrations are remarkably consistent between two samples taken from the (Na, Ca) Cl experiment and likewise comparable to results from the (Na,K) Cl experiment, indicating overall excellent repeatability of sampling and analytical methods (Table 3). Most transition metals investigated (V, Cr, Mn, Fe, Co, Ni, Cu, Zn, and Cd) are present in higher concentrations in the (Na,Ca) Cl reaction fluid than in the (Na,K) Cl reaction fluid, whereas W concentrations are higher in the (Na,K) Cl reaction fluid, and Mo concentrations are generally the same in fluids from both experiments. The major fraction of transition metals present in the experimental system remains in the solid, however, with typical extraction efficiencies < 5% (Table 4). The extraction efficiency of Mn is somewhat higher than other transition metals investigated; 7% in the (Na,K) Cl experiment and 15% in the (Na,Ca) Cl experiment. For comparison, the extraction efficiency of the highly soluble Li and K are 78–85% and 85–91%, respectively (Table 4).

Where comparable data exist (Mn, Fe, Cu, Zn), fluid metal concentrations resemble those collected from previous 350 °C reaction experiments (Seyfried and Janecky, 1985; Seewald and Seyfried, 1990). Other

elements—V, Cr, Co, Ni, Mo, Cd, and W— have not been previously measured in reactions fluids from hydrothermal basalt alteration experiments but are generally consistent with expectations based on measurements of natural seafloor hydrothermal fluids (e.g., James et al., 1995; Metz and Trefry, 2000; Diehl and Bach, 2020 and references therein; Evans et al., 2023).

## 3.3. Micro-XRF and XANES analyses

Molybdenum was not detected in  $\mu$ -XRF maps of unreacted BEPR. Attempted Mo k-edge XANES spot analyses of Ti-rich (magnetite), Rb-rich (glass), and Cu- and S-rich (sulfide) regions of spectral maps did not yield distinct Mo k-edge adsorption edges except for a few poorly resolved absorption edges on Ti-rich spots, indicating that Mo concentrations are below or at most similar to the estimated detection limit of  $\sim 10~\mu g/g$ .

In contrast, Mo was detected in  $\mu$ -XRF maps of altered BEPR samples from the (Na,Ca)Cl experiment as numerous Mo-rich particles with cross-sectional diameters of ~10  $\mu$ m (Fig. 4). Mo-XANES spectra from these spots exhibit clear Mo adsorption edges (Fig. 6), definitively

**Table 3**Measured chemistry of hydrothermal reaction fluids. 'bql is below the quantitative limit, or 10 standard deviations above blank levels.

		BEPR 350 (	BEPR 350 (Na,K)Cl		BEPR 350 (Na,Ca)Cl			
		Starting Fluid	Reaction Fluid	Starting Fluid	Reactio	n Fluid		
Duration	days	0	50	0	53	55		
Temp. Fluid: Rock	C g/g	25 0.98	350 0.76	25 1.1	350 1.1	350 0.85		
pH	at 25 C		5.9		5.4	5.5		
pН	at		6.2		5.6	5.6		
$H_2$	350 C mmol/ kg		0.23		0.47	0.31		
$H_2S$	mmol/ kg		3.57		3.12			
Cl	mmol/ kg	547	547	491	491	491		
Na	mmol/ kg	537	504	402	437	438		
Mg	mmol/ kg		0.01		0.03	0.03		
K	mmol/ kg	10.0	33.9		25.7	25.7		
Ca	mmol/ kg		4.5	44.6	15.0	14.5		
Si	mmol/ kg		19.2		22.9	23.0		
Al	mol/ kg		15.6		34.4	33.9		
Transition 1	Metals							
V	nmol/ kg	1.6	191	48	715	299		
Cr	mol/ kg	0.001	1.8	0.08	12.0	12.6		
Mn	mol/ kg	0.03	15.6	0.007	34.4	33.9		
Fe	mol/ kg	0.1	62.2	0.8	160	256		
Co	nmol/ kg	2	bql	32	64.5	281.4		
Ni	mol/ kg	0.001	2.7	0.1	20.0	22.7		
Cu	mol/ kg	0.01	3.2	0.1	62.6	10.0		
Zn	mol/ kg	0.001	5.9	0.1	11.9	8.7		
Мо	nmol/ kg	14	801	3	797	775		
Cd	nmol/ kg	0.08	23.9	4.5	82.1	60.7		
W	nmol/ kg	9.3	143	1	86	73		
Trace Alkal	i Metals							
Li	mol/ kg		270		247	253		
Rb	mol/ kg		15.1		15.9	15.9		
Cs	nmol/ kg		96.7		110.1	106.9		

confirming the presence of Mo. Molybdenum was also detected in -XRF maps of altered seafloor basalt from Pito Deep Rift (Fig. 5). As with the experimental sample, Mo occurs as small Mo-rich particles that yield clear Mo k-edge adsorption peaks (Fig. 6). Unfortunately, the small size of these particles, which approached the spatial precision of the sampling stage, and limited analytical time precluded collection of sufficient spectra to definitively identify the Mo phase relative to measured standards. Altered basalt from the (Na,K)Cl experiment was not analyzed based on similar limitations.

Table 4
Extraction efficiencies of transition metal elements and selected alkali metals based on measured elemental compositions of EPR basalt (Table 1), fluid chemistry (Table 3) and a starting fluid:rock ratio of 1:1.

Extraction Efficiency				
	(Na,K)Cl fluid	(Na,Ca)Cl fluid		
V	0.00%	0.01%		
Cr	0.03%	0.19%		
Mn	7%	15%		
Fe	0%	2%		
Co		0%		
Ni	0.2%	1%		
Cu	0.2%	4%		
Zn	1%	2%		
Mo	2.2%	2%		
Cd	1%	2%		
W	5%	3%		
Li	85%	79%		
Rb	60%	63%		
Cs	68%	77%		
K	85%	91%		

#### 3.4. Molybdenum solubility calculations

Calculations of aqueous speciation based on thermodynamic data contained in the employed 500-bar database (Section 2.5) indicate that in situ pH is p $H_{350\ C}$  6.2 for the (Na,K)Cl reaction fluid and p $H_{350\ C}$ 5.6 for the (Na,Ca)Cl reaction fluid (Table 3). Based on measured H2 and H<sub>2</sub>S, both fluids are calculated to be in the magnetite stability field and saturated with respect to magnetite, quartz, chalcopyrite, bornite, pyrrhotite, molybdenite, and numerous silicate minerals associated with hydrothermal environments including epidote, clinozoisite, plagioclase solid solutions, and hedenbergite. The predicted dominant species of Mo at in situ conditions is NaHMoO4. Calculated Mo solubility with respect to molybdenite is 283 nmol/kg for the (Na,K) Cl reaction fluid and 69 nmol/kg for the (Na,Ca) Cl reaction fluid. These predictions are significantly less than measured values of 801 nmol/kg and 775 797 nmol/kg for the (Na,K) Cl and (Na,Ca) Cl experiments, respectively, and indicate that solubility models contain a pH dependence of Mo solubility that is not observed in experimental reaction fluids.

#### 4. Discussion

#### 4.1. Transition metals in hydrothermal fluids

Previous experimental studies designed to reproduce seafloor hydrothermal fluids suggest that transition metal concentrations, and the effects of fluid temperature, salinity, pH, and other chemical parameters (e.g.,  $f_{O_2}$ ,  $f_{S_2}$ ) can be attributed to a near-equilibrium chemical states achieved between high-temperature aqueous fluids and buffering mineral assemblages. Examples include magnetite chlorite amphibole for Mn and Fe (Seyfried and Ding, 1995; Pester et al., 2011) and chalcopyrite for Cu (Seyfried and Ding, 1993). Transition metal concentrations in seafloor vent fluids are additionally controlled by near surface processes that deposit or remobilize seafloor or subseafloor sulfide deposits, as demonstrated by analyses of fluids from the TAG hydrothermal field on the Mid-Atlantic Ridge (Tivey et al., 1995) and the 2019 2020 series of vent fluids collected from Main Endeavour Field (Evans et al., 2023), among numerous other studies of seafloor vent fluids (e.g., Hannington et al., 1998; Petersen et al., 2005; Klose et al., 2022).

## 4.1.1. Chloride complexed transition metals

Thermodynamic data indicate that many transition metals, including Mn, Fe, Ni, Co, Cu, Zn, and Cd, occur as neutral chloride complexes at *in situ* hydrothermal conditions. Dissolution of such metals can be represented by the equation:

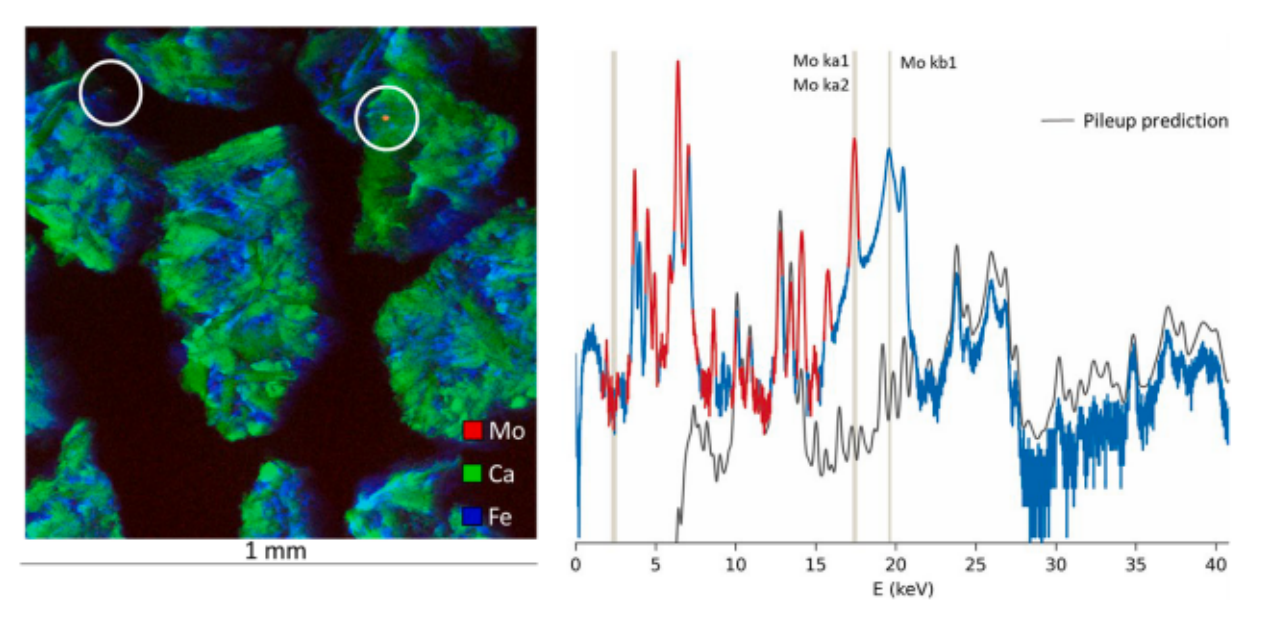


Fig. 4. Left Image: Micro XRF map of experimentally altered basalt based on an incoming beam energy of 20 keV. Color scheme is Mo (red.), Ca (green), Fe (blue). While circles highlight Mo-rich spots (red.). Additional prominent minerals in micro XRF map are plagioclase (dark green), pyroxene (bright green) and magnetite (blue). Right Image: A representative XRF spectrum of Mo-rich spot (right) exhibits clearly distinguished Mo ka and kb1 fluorescence peaks as well as predictions of sensor pile-up (pileup prediction) caused by multiple photon impacts on the detector between readouts. (For interpretation of the references to color in this figure legend, the reader is referred to the web version of this article.)

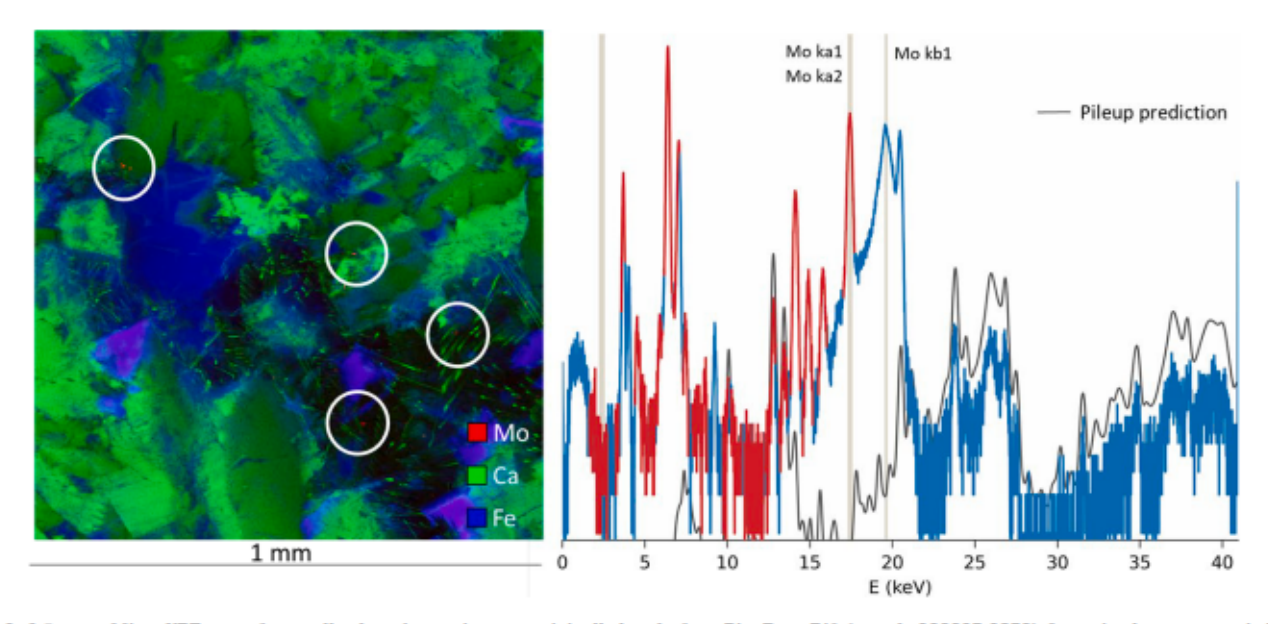


Fig. 5. Left Image: Micro XRF map of naturally altered oceanic crust, originally basalt, from Pito Deep Rift (sample 022205-0852). Incoming beam energy is 20 keV. Color scheme is Mo (red), Ca (green), Fe (blue). While circles highlight Mo-rich spots (red). Additional prominent minerals in micro XRF map are amphibole (dark green), chlorite (bright green) and sulfides (blue-purple). Detection of elevated florescence in the Mo ka band on sulfides is attributable to pileup of Zn ka florescence and does not clearly indicate presence of Mo. Follow-up Mo k-edge XANES on these minerals did not reveal a Mo adsorption edge, suggesting Mo concentration < 10 µg/g, if present. Right Image: A representative XRF spectrum of Mo-rich spot exhibits clearly distinguished Mo ka and kb1 fluorescence peaks. "Pileup prediction" is the expected background interference caused by multiple impacts of lower energy photons. (For interpretation of the references to color in this figure legend, the reader is referred to the web version of this article.)

$$nH^+ + nCl^- + Me_{n/2}O_{(s)} \leftrightarrow MeCl_{n(aq)} + H_2O$$

where  $Me_{n/2}O_{(4)}$  represents a metal component of an oxide or silicate mineral, n is the charge of the metal cation and  $MeCl_{n(aq)}$  is the neutral chloride complex in solution (Pokrovski et al., 2008; Xing et al., 2021). Thus, these metals are predicted to be more soluble in lower pH, higher salinity (i.e., chlorinity) fluids. Dissolution of metal sulfide minerals can be analogously represented:

$$nH^+ + nCl^- + Me_{n/2}S_{(s)} \leftrightarrow MeCl_{n(aq)} + H_2S$$

which introduces a reduced-sulfur dependence. Consistent with the predicted pH dependence, concentrations of chloride-complexed transition metals are higher in the lower pH reaction fluids from the (Na, Ca) Cl experiment, an observation which conversely confirms the *in situ* pH difference between the two experiments predicted by aqueous speciation models.

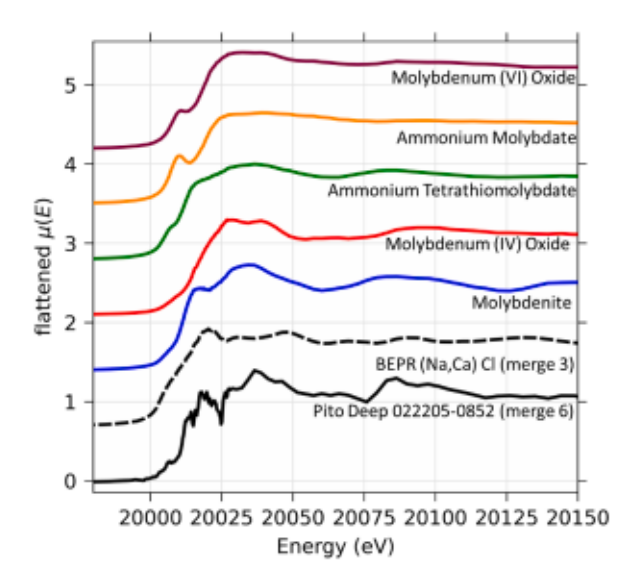


Fig. 6. Merged XANES spectra of Mo-rich spots in experimentally altered East Pacific Rise basalt (BEPR) and Pito Deep sample 022205-0852 compared with Mo standards. Merge 3 and merge 6 are an averaging of 3 and 6 collected spectra, respectively, following detrending and normalization based on the magnitude of the adsorption-edge.

## 4.1.2. Molybdenum solubility equations

Previous studies have indicated that Mo mass balance in basalt is controlled by volcanic glass (quenched melt) and Fe-Ti oxides: magnetite and ilmenite (Greaney et al., 2017; Greaney et al., 2018), where it occurs in +6 valance bonded to oxygen (O'Neill and Eggins, 2002; Danielson et al., 2011). Compiled thermodynamic data and resultant aqueous speciation models at in situ hydrothermal conditions indicate that Mo occurs in +6 valance as part of the molybdate oxyanion, MoO<sub>4</sub><sup>2-</sup>, which can be variably complexed with available cations, H<sup>+</sup> and Na<sup>+</sup>, and that hydrothermal fluids are saturated with respect to molybdenite.

Written to the predicted dominant aqueous species, dissolution of molybdenite can be represented by the following formula:

$$Na^{+} + 4H_{2}O + MoS_{2} = NaHMoO_{4(aq)} + 2H_{2}S + H_{2} + H^{+}$$

Hence, it is expected that Mo will be more soluble under higher pH, less reducing, less sulfidic conditions. A salinity dependence is also expected, albeit because of the increased activity of Na<sup>+</sup>, rather than Cl<sup>-</sup>. The expected solubility of Mo in response to fluid pH and redox conditions contrasts with that of Fe, which is more soluble under acidic, more reducing conditions (Fig. 7).

Previous experimental studies of molybdenite solubility under roughly similar physical-chemical conditions (0.5 mol/kg NaCl fluid reacting with molybdenite and a pyrite-pyrrhotite-magnetite (Py-Po-Mag) mineral buffer at 350 °C) have reported equivalent or greater Mo concentrations of up to ~3200 nmol/kg (Wood et al., 1987; Cao, 1989) and have demonstrated the expected increase in Mo solubility in response to lower reduced sulfur concentrations (Cao, 1989). Unfortunately, direct comparisons of current results with these previous experiments are limited by uncertainties surrounding the *in situ* conditions of previous experiments (e.g., pH, redox) and sensitivity and accuracy of the analytical and sampling techniques available at the time with respect to Mo.

Molybdenite-saturated Mo concentrations calculated using currently available thermodynamic data (see Section 3.3.) are roughly 3–10 times less than experimental results and suggest a pH dependence of molybdenite solubility that is not observed in experimental fluids. The greater solubility and apparent lack of pH dependence observed in experiments relative to thermodynamic models invites the possibility of additional dissolved Mo species not yet included in thermodynamic models. For example, it has been previously proposed that Mo occurs as



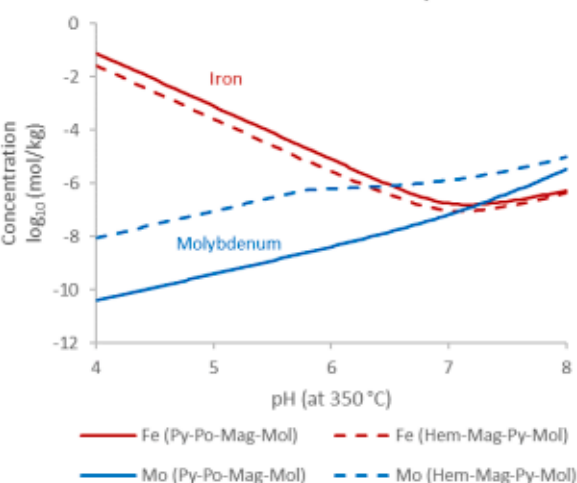


Fig. 7. Solubility of Mo and Fe at 350 °C, 500 bars as a function of fluid pH in fluids in the presence of the pyrite-pyrrhotite-magnetite-molybdenite (Py-Po-Mag-Mol) and hematite-magnetite-pyrite-molybdenite (Hem-Mag-Py-Mol) mineral buffers as calculated by GWB React module. Fluid Na and Cl concentrations = 500 mmol/kg.

thiomolybdate species (MoO<sub>(x)</sub>S $^{2-}_{(4-x)}$ ) in sulfidic aqueous environments (Erickson and Helz, 2000). However, high-temperature experiments indicate that MoS $^{2-}_4$  is only prevalent at high temperatures (e.g., 286 °C) if sulfide concentrations >1 mol/kg (Liu et al., 2020), far greater than the <1–20 mmol/kg range of seafloor hydrothermal vent fluids (Diehl and Bach, 2020) or analog experiments (e.g., Seewald and Seyfried, 1990). It is worth noting, however, that the experiments of Liu et al, (2020) were conducted at vapor-saturated pressure. Hence, thermodynamic data for thiomolybdate species at the higher pressures and temperatures relevant to seafloor hydrothermal systems and analog experiments are not well constrained.

Alternatively, Cao (1989) proposes the existence of a Mo(+5) aqueous species, MoO(OH)<sub>2</sub>Cl, based on empirical observations of "molybdenum blue" in hematite-magnetite (Hem-Mag) buffered experiments, and additional Mo solubility experiments containing Hem-Mag, hematite-magnetite-pyrite (Hem-Mag-Py), and Py-Po-Mag mineral-buffer assemblages. Inclusion of MoO(OH)<sub>2</sub>Cl in thermodynamic calculations based on the reaction coefficients proposed by Cao (1989) (Table 5) results in calculated molybdenite-saturated Mo concentrations of 299 nmol/kg in (Na,Ca)Cl reaction fluids and 137 nmol/kg in (Na, K) Cl reaction fluids. In addition to increasing the Mo solubility, MoO (OH)<sub>2</sub>Cl (or any other Cl<sup>-</sup> complex) acts to mitigate the pH dependence

Table 5 Compiled thermodynamic data for Mo species at 350 °C.

React	ion	Log K
(1)	$MoS_2 + 3H_2O + 4.5 O_2 = MoO_4^2 + SO_4^2 + 6H^+$	79.7639*
(2)	$MoO_2 + H_2O + 0.5 O_2 = MoO_4^{2-} + 2H^+$	-2.3285*
(3)	$MoO_3 + H_2O = MoO_4^{2-} + H^+$	-11.6199*
(4)	$HMoO_{4}^{-} = H^{+} + MoO_{4}^{2-}$	-7.3491 <sup>b</sup>
(5)	$H_2MoO_4 = 2H^+ + MoO_4^{2-}$	-8.464 <sup>b</sup>
(6)	$NaHMoO_4 = Na^+ + H^+ + MoO_4^{2-}$	-9.4721°
(7)	$MoO(OH)_2Cl = MoO_2 + 0.25 O_2 + H^+ + Cl^- + 0.5 H_2O$	$-10.60^{d}$
(8)	$MoO(OH)_2Cl + 0.5 H_2O + 0.25 O_2 = MoO_4^{2-} + 3H^+ + Cl^-$	-12.9285°

Thermodynamic data for basis species MoO<sub>4</sub><sup>2-</sup> from Shock et al. (1997).

- Robie and Hemingway (1995), Reaction coefficients calculated with HCh.
- b Minubayeva and Seward (2010), Reaction coefficients calculated with HCh.
- <sup>e</sup> Shang et al. (2020), Reaction coefficients calculated with HCh.
- d Cao (1989).
- <sup>6</sup> Calculated from reactions 2 and 7.

of molybdenite solubility as pH drives solubility in the opposite directions for the two proposed reactions:

$$Na^{+} + 4H_{2}O + MoS_{2} = NaHMoO_{4(aq)} + 2H_{2}S + H_{2} + H^{+}$$

$$H^+ + 3H_2O + MoS_2 + Cl^- = MoO(OH)_2Cl + 2H_2S + \frac{1}{2}H_2$$

To the best of our knowledge, the existence and thermodynamic properties of this and other potential Mo(+5) aqueous complexes have not been rigorously investigated. So far, published studies and experiments aimed at deriving thermodynamic data for aqueous Mo species focus exclusively on Mo (+6) species. Consequently, experimental fluids are typically more oxidizing than Hem-Mag, itself highly oxidizing in the context of natural seafloor hydrothermal systems. Considering that current thermodynamic data significantly underestimate fluid Mo concentrations in these and previous hydrothermal experiments conducted at Hem-Mag-buffered and more reducing conditions, there is a need for further investigations to identify aqueous Mo species under such conditions and, if identified, to derive the relevant thermodynamic data. In the meantime, some caution is warranted in extrapolating experimental results to vastly different temperatures or chemical conditions using currently available thermodynamic models.

#### 4.2. Molybdenum in modern seafloor vent fluids

#### 4.2.1. Historical samples

Previous samples collected from basalt-hosted vent fields, Cleft Segment (Trefry et al., 1994), TAG hydrothermal mound (Metz and Trefry, 2000), Main Endeavour Field (Seyfried et al., 2003), contain variable Mo concentrations, but are typically depleted relative to seawater (Fig. 8). One exception is a 363 °C fluid containing 148 nmol/kg Mo collected from the TAG hydrothermal mound, a large hydrothermal deposit on the Mid-Atlantic Ridge (Metz and Trefry, 2000). However, these samples also contain variable and often significant concentrations of Mg, indicative of mixing with seawater and probable loss of Mo during/prior to sampling. Samples collected from the felsichosted Roman Ruins vent field, Manus Basin, used by Miller et al. (2011) to develop a model of Mo geochemical cycling in modern surface environments, likewise exhibit variable Mg concentrations indicative of

seawater mixing prior to sampling and, consequently, probable loss of Mo.

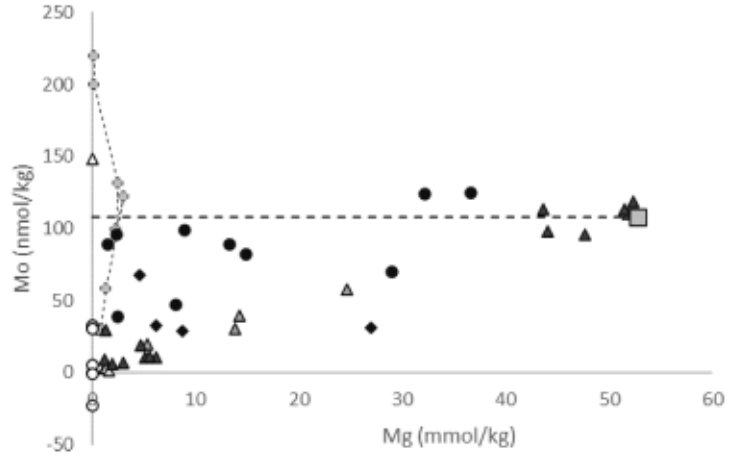
Samples collected from ultramafic-hosted sites, Rainbow (Douville et al., 2002), Logatchev (Schmidt et al., 2007), and Niebelungen (Schmidt et al., 2011), contain low concentrations of Mo and extrapolate to consistently low zero-Mg endmember concentrations supported by low Mg samples (Fig. 8). While these samples are not immune to the sampling artifacts mentioned above, the lack of any samples with elevated Mo concentrations and extrapolation to a consistent endmember suggests these high-temperature ultramafic-hosted vent fluids are in fact depleted in Mo.

Greater-than-seawater Mo concentrations have also been reported in low-temperature hydrothermal fluids including Baby Bare (Mo =  $297 \pm 3 \text{ nmol/kg}$ , Wheat et al., 2002) and Dorado Outcrop (Mo =  $126 \pm 2 \text{ nmol/kg}$ , Wheat et al., 2017). However, these fluids contain significant concentrations of sulfate and negligible sulfide, indicative of generally oxidizing conditions under which Mo is expected to be quite soluble and geochemical processes distinct from those most relevant to high-temperature hydrothermal circulation. While these low-temperature fluids are not discussed further in this paper, they should be considered for further study of Mo cycling under lower-temperature, intermediate redox conditions.

## 4.2.2. Main endeavour field 2019-2020 time series

Recently, a time series of nine vent fluid samples was collected from October 2019 to May 2020 from a 281–304 °C vent at Main Endeavour Field on the Juan de Fuca Ridge (hereafter, MEF 2019–2020) (Seyfried et al., 2022). These samples are unique among seafloor vent fluid samples in that ambient Mg- and Mo-rich seawater was entirely excluded from the collected samples during sampling and repeat samples could be obtained at month-long intervals (Seyfried et al., 2022; Evans et al., 2023). These samples, which include analyses of vent fluid sampler precipitate fractions, contain 29–220 nmol/kg Mo, with 4 of 9 samples enriched in Mo relative to seawater (Fig. 9, Evans et al., 2023).

That greater-than-seawater Mo concentrations are found in moderately high-temperature vent fluids clearly demonstrates that basalthosted seafloor vent fluids can be net source of Mo to modern ocean environments. Moreover, a detailed analysis of MEF 2019–2020 samples sheds light on the response of Mo concentrations to changes in the



- S. Cleft (Trefry et al., 1994)
- Main Endeavour Field (Seyfried et al., 2003)
- --- Ф--- MEF 2019-2020 Time Series (Evans et al., sub.)
  - △ TAG (Metz and Trefry, 2000)
  - ▲ Rainbow (Douville et al., 2002)
  - ▲ Logatchev (Schmidt et al., 2007)
  - Nibelungen (Schmidt et al., 2011)
  - Roman Ruins (Miller et al., 2011)
  - Seawater

Fig. 8. Published analyses of Mo in seafloor vent fluids indicate that vent fluid samples are typically depleted in Mo relative to ambient seawater. These data also illustrate the difficulty in obtaining vent fluid samples uncontaminated by Mo-rich seawater, with the extent of seawater entrainment during sampling indicated by Mg concentrations. A time series of fluid samples collected from Main Endeavour Field (2019–2020) includes several samples with Mo concentrations greater than seawater (Evans et al., 2023). Samples from this time series with the most Mo contain among the lowest Mg concentrations yet reported for seafloor vent fluid samples. Unlike other data shown in the figure, data from Trefry et al. (1994) and Metz and Trefry (2000) are endmember values extrapolated to zero Mg, a technique best suited to determining concentrations of elements that behave conservatively during hydrothermal fluid-seawater mixing (Von Damm et al., 1985). This technique occasionally results in negative values attributable to non-conservative behavior of Mo as vent fluids cool and/or mix with seawater the comparatively high concentrations of Mo in seawater. Actual samples contained higher Mg concentrations (Butterfield and Massoth, 1994). All data shown include analyses of sampler precipitate fractions.

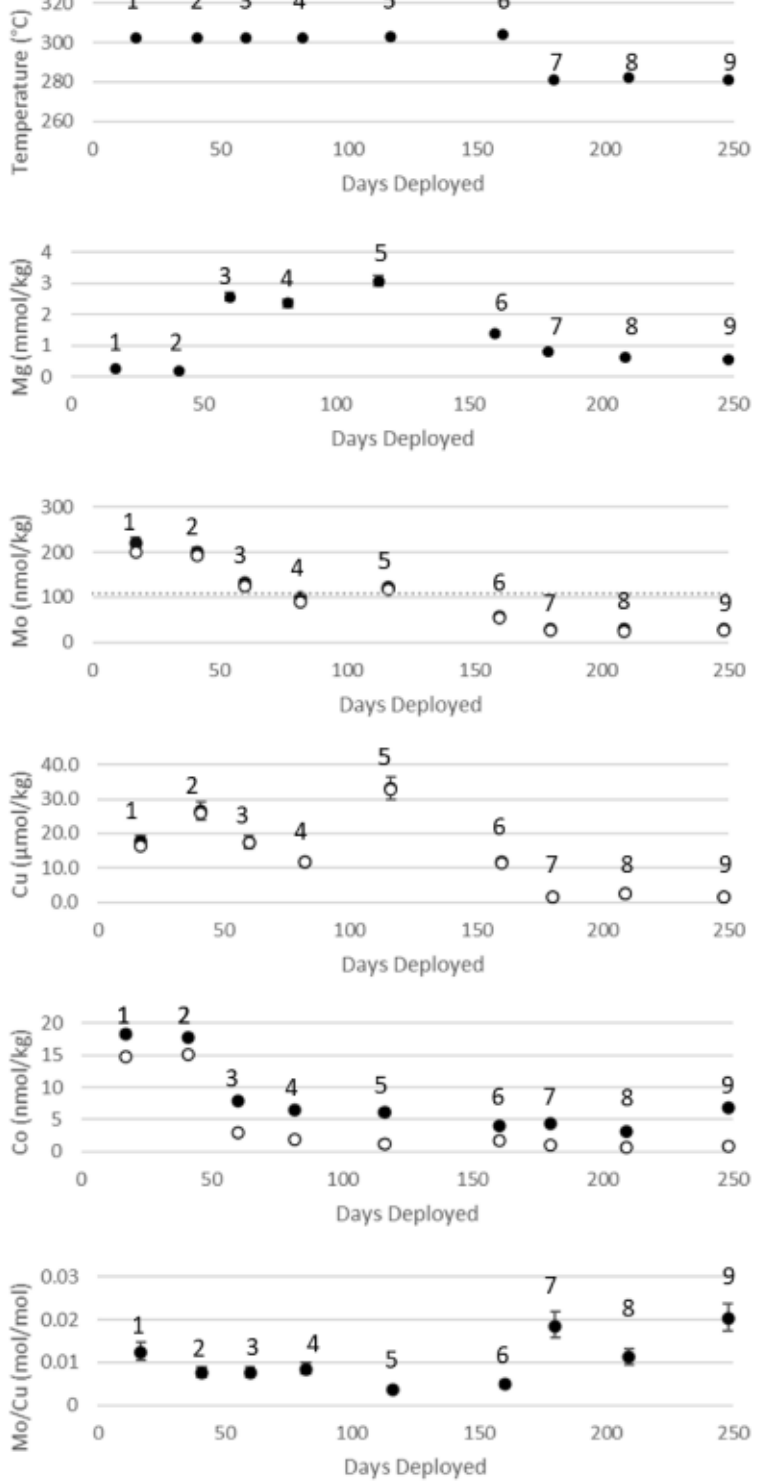


Fig. 9. Temperature, Mg, Mo, Cu, Co concentrations, and Mo:Cu molar ratios in a time series of vent fluids obtained from Main Endeavour Field. Low Mg concentrations in samples 1–2 and 7–9 suggest that these samples are least affected by entrainment of the reacted seawater component that affected samples 3 to 6, and thus most closely reflect high-temperature hydrothermal reactions. Numbers above data points are sample numbers referred to in the text. Concentrations of Mo, Cu, and Co attributable to sampler precipitate fractions are displayed in white. Reconstructed fluid concentrations are displayed in black. Gray stippled line on Mo graph indicates seawater Mo = 108 nmol/kg.

hydrothermal system.

Samples 1 and 2 vented at 302 °C and contain 220-200 nmol/kg Mo and 0.24-0.19 mmol/kg Mg, respectively (Fig. 9). These low Mg concentrations are comparable to those of hydrothermal experiments, suggesting these samples are uncontaminated by surrounding seawater. Samples are highly supersaturated with respect to molybdenite, suggesting that Mo concentrations reflect equilibration at higher temperature conditions, as is the case for Fe, Mn, Si, Cl, and indeed most fluid components (Seyfried et al., 2022).

Samples 3-6 contain 58-132 nmol/kg Mo and 1.39-3.07 mmol/kg

Mg (Fig. 9). While vent fluid temperatures exhibit no change over this period (302–304 °C), the addition of a Mg-containing fluid in the subsurface clearly effects Mo concentrations, as well as Co, which decreases from 18 nmol/kg in samples 1 and 2 to 4.0–7.8 nmol/kg in samples 3–6 (Fig. 9). Based on an observed depletion of sulfate relative to Mg attributable to subsurface anhydrite precipitation, Seyfried et al. (2022) propose that the Mg-containing fluid represents an incursion of heated (>150 °C) partially equilibrated seawater rather than contamination by ambient cold (~2 °C) seawater very close to the vent orifice. Such an incursion could represent a cooling event deeper in the system that

enhances precipitation of temperature-sensitive (i.e., supersaturated) elements like Mo and Co, with little or no effect on seafloor vent fluid temperatures.

The temperature dependence of Mo and other transition metals (except Mn) is also evident in samples 7-9, which were collected at 281-282 °C following an abrupt decrease in vent fluid temperature (Fig. 9). Importantly, samples 7-9 contain 0.56-0.8 mmol/kg Mg, suggesting that the influx of Mg-containing fluid and its accompanying effects had largely dissipated by this time. Hence, a clear temperature dependence can be observed in which samples 7-9 collected at 281-282 °C contain = 29-30 nmol/kg Mo and samples 1-2 collected at 302 °C contain 200-220 nmol/kg Mo (Fig. 9). The 350 °C experimental reaction fluids containing 775-801 nmol/kg Mo qualitatively continue the observed positive trend between vent fluid temperature and Mo concentrations, as previously proposed by Metz and Trefry (2000). The molar ratio of Mo to Cu, another temperature-sensitive element, is  $3.6-19 \times 10^{-3}$  in fluid sample precipitate fractions and  $3.7-19 \times 10^{-3}$  in reconstructed fluids. The similarity in these ratios reflects that the vast majority of Mo (86-96%) and Cu (93-100%) is contained in sampler precipitate fractions (Evans et al., 2023).

#### 4.2.3. Main endeavour field sediment traps

Sediment trap samples from Main Endeavour Field contain 9–66  $\mu$ g/g Mo and 0.18–1.2 wt% Cu (Coogan et al., 2017, Fig. 10). Significantly, the molar Mo:Cu ratio in sediment trap samples (Mo:Cu = 3.1–5.6  $\times$  10<sup>-3</sup>, Fig. 10) closely resembles that of MEF 2019–2020 vent fluids and

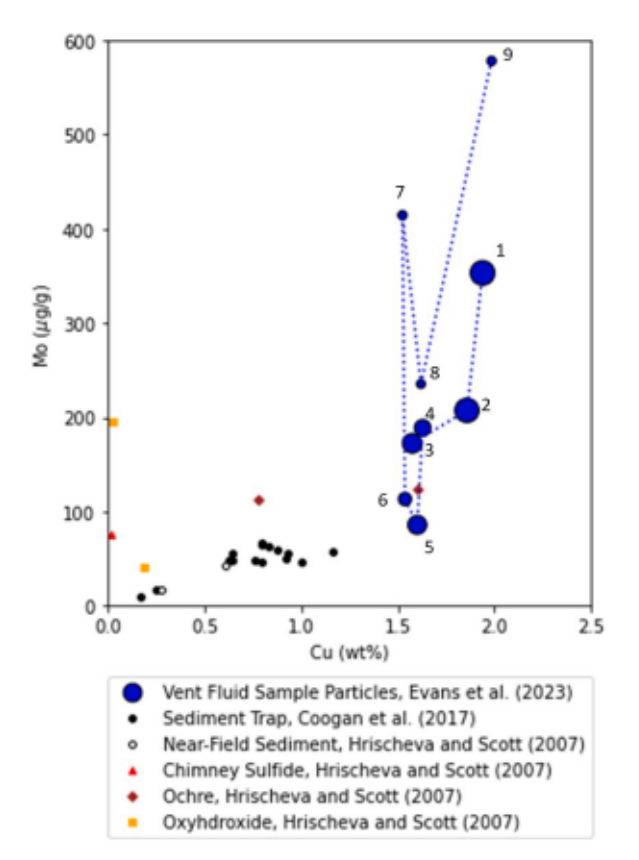


Fig. 10. Plot of Cu vs. Mo concentrations in Main Endeavour Field seafloor sulfide deposits, sediments, and sediment trap samples compared with concentrations in sampler precipitates from the Main Endeavour Field 2019–2020 time series sampling. Data from Hrischeva and Scott (2007) include samples from Mothra Vent Field, also on the Endeavour Segment of the Juan de Fuca Ridge. The total mass of fluid sample particulates was estimated by adding equimolar concentrations of sulfur to analyzed metals (dominantly Fe and Zn). Marker sizes for fluid sampler precipitates are scaled to fluid Mo concentrations (Fig. 9; Evans et al., 2023).

fluid precipitate fractions resemble the hydrothermal component of sediment trap samples, which is enriched in Mo and Cu (Fig. 10). Weathered seafloor deposits collected by Hrischeva and Scott (2007) (Fig. 10) exhibit generally higher Mo:Cu ratios than sediment trap samples, consistent with adsorption of Mo from surrounding seawater and/or preferential dissolution of Cu during oxidative seafloor weathering.

Previous analyses of sediment trap samples and seafloor sediments demonstrate that Cu concentrations in sediments decrease sharply with distance from Endeavour Segment vent fields, including Main Endeavour Field. This pattern was initially interpreted to indicate that much of the Cu emitted by MEF hydrothermal vent fluids is deposited in the near-field environment (Hrischeva and Scott, 2007). However, more recent mass balance estimates based on denser samplings of sediment trap- and seafloor sediment samples indicates that, in fact, <2% of Cu emitted by MEF vent fluids is deposited within 1.5 km of the vent field (Coogan et al., 2017).

The observation that Mo:Cu ratios in sediment trap samples closely resemble those of hydrothermal vent fluids leads to two surprising conclusions. First, that much of the Mo in near-field sediment traps is directly derived from hydrothermal fluids rather than adsorption of seawater Mo onto hydrothermal plume particles. Second, the lack of preferential enrichment of Mo in sediment trap samples relative to Cu suggests that much of the Mo delivered to the ocean by hydrothermal vent fluids may be transported out of the near-vent field, as previously demonstrated for Cu.

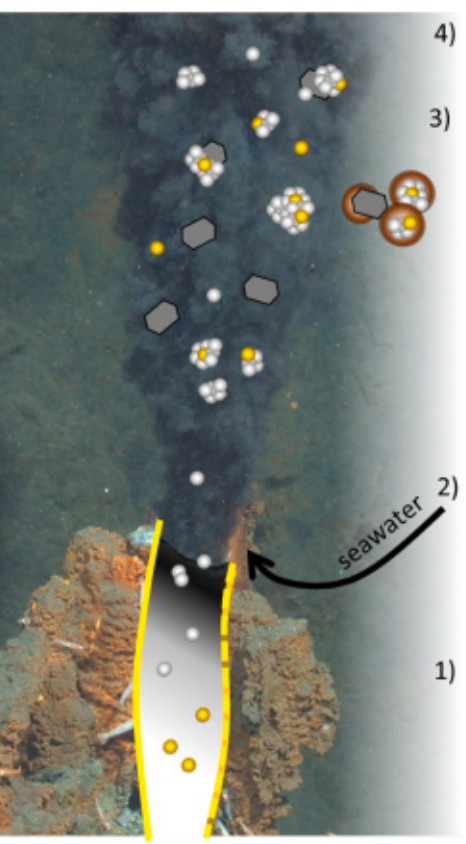
Findlay et al. (2019) outline a model for hydrothermal plume particle formation in the first few meters of the buoyant plume. Based on this model, nanoparticulate (<200 nm) pyrite forms in first ~10 cm of plume and persists within the buoyant plume such that it is ultimately advected from the near-vent system. Higher in the plume, larger metal sulfide particles form and preferentially settle (Findlay et al., 2019). Analyses of hydrothermal plume particles in the first 1.5 m of buoyant plumes emanating from the TAG, Snakepit, and Rainbow hydrothermal field on the Mid-Atlantic Ridge, as well as plume particles derived from various hydrothermal fields in the Lau Basin (southwest Pacific Ocean) yield observations of nanoparticulate pyrite and chalcopyrite and associated correlations between Co, Cu, and Fe concentrations (Gartman et al., 2014; Findlay et al., 2015).

Samples of near-vent seafloor sediments collected at MEF contain fine-grained (<10 µm) sulfide particles as components of larger (<300 µm) crystalline and colloform aggregates bound by Mn- Fe- Si-rich gel (Hrischeva and Scott, 2007). Considering the model of Findlay et al. (2019), these particles likely formed in the first few meters of the buoyant hydrothermal plume before settling out as near-vent sediments, which, in the case of fine-grained particles, was likely facilitated by particle aggregation. Our data indicate that Mo/Cu ratios are preserved throughout the venting and settling process. We therefore propose that Mo precipitates early in the venting process, entering the ocean or hydrothermal sediments as nanoparticulate material (Fig. 11). Analogous to Cu, most of this material is advected out of the near-vent field. However, a small fraction is aggregated into larger particles and settles near the vent.

## 4.3. Molybdenum in subseafloor hydrothermal systems

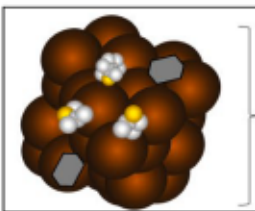
Analyses of Mo in altered oceanic crust from Pito Deep Rift indicate variable enrichments and depletions of Mo (Zhu. 2016, Fig. 2B), consistent with variable hydrothermal extraction and deposition of Mo in the subsurface. Synchrotron-based µXRF maps and Mo-kedge XANES of the Mo-enriched sample, 022205-0852, identify Mo-rich particles. The location of this sample deep within the hydrothermal system and occurrence of rare fine-grained Mo-rich particles is consistent with Mo enrichment occurring through precipitation of molybdenite from high-temperature hydrothermal fluids.

Experimentally altered BEPR also contains Mo-rich particles,



4) A large fraction of vent fluid Mo and Cu escapes settling and is advected out of the near-vent environment.

3) Continued mineral growth and particle aggregation in the hydrothermal plume leads to differential settling of particles. Original Mo/Cu ratio is preserved by incorporation of earlyformed Mo- and Cu-rich particles into larger settling aggregates.



Sediment trap sample comprising aggregated metal 100 um sulfide particles and Mn-Fe-Si-rich gel phase (brown) (Hrischeva and Scott, 2007).

Mixing with seawater increases pH, causing precipitation of larger (> 200 nm) Fe- and Zn- rich metal sulfide particles and silicate minerals (Findlay et al., 2019). Addition of sulfate leads to formation of barite, anhydrite (Gartman et al., 2014).

Zinc sulfide

1) Rapid cooling at or near venting induces precipitation of Moand Cu-rich nanoparticles. Nanoparticles (< 200 nm) include pyrite and chalcopyrite (Gartman et al., 2014).

- Nanoparticulate pyrite
- Nanoparticulate chalcopyrite

Fig. 11. Summary diagram of particle formation in the buoyant hydrothermal plume.

likewise of uncertain identity, in contrast to unaltered BEPR, where the lack of Mo-k-edge XAS adsorption edges despite 3.3 µg/g Mo measured in bulk samples suggests that Mo is widely distributed, presumably as a component of quenched melt and titanium-bearing magnetite.

The occurrence of Mo-enriched, molybdenite-containing samples below the lava-dike transition zone at Pito Deep Rift resembles analyses of pyrite in drill cores from the active TAG hydrothermal field, where Mo is enriched in the subsurface stockwork zone and where transient peaks in Mo concentrations during laser-ablation analysis of sulfide minerals (pyrite and chalcopyrite) in the stockwork are attributed to the presence of >30 µm Mo-rich inclusions (Grant et al., 2018). The association of molybdenite with the higher-temperature regions of hydrothermal systems is also well known in porphyry copper deposits, where Cu-Mo enriched zones occur in the central, highest-temperature regions of the deposits (e.g., Sillitoe, 2010). Coupled Mo and Cu mobility has also been reported in the 3.6-3.2 Ga age volcanic-hosted seafloor hydrothermal systems of the Panorama district (Huston et al., 2001).

Hence, a conceptual model can be developed in which Mo, originally present in volcanic glass, magnetite, ilmenite, and potentially seawater, is extracted by high-temperature hydrothermal fluids and reprecipitated as molybdenite deep within the hydrothermal system. Accordingly, concentrations of Mo in hydrothermal vent fluids should reflect the solubility of molybdenite in the context of rock-dominated fluid-rock reactions that buffer fluid pH,  $f_{O_2}$ , and  $f_{S_2}$  and salinity that reflects seawater and subsurface phase separation (e.g., Seyfried and Ding, 1995).

## 4.3.1. Molybdenite solubility as a function of temperature, H<sub>2</sub>S, and H<sub>2</sub>

Samples of natural and experimental hydrothermal fluids and the location of the Mo-enriched samples at Pito Deep Rift deep within the hydrothermal system indicate that Mo concentrations in hydrothermal fluids are highly sensitive to temperature. Chemical equations for hydrothermal molybdenite precipitation indicate additional dependences

on fluid sulfur content and redox states. To construct a model by which to calculate molybdenite solubility for "typical" basalt-hosted hydrothermal fluids, we start with average vent fluid concentrations of major elements - Cl, Na, K, and Ca- as compiled by Diehl and Bach (2020). For simplicity, and because the presence of K+ is not predicted to significantly modify the chemical behavior of the system, we assume that K+ can be effectively modeled as additional Na<sup>+</sup> and then adjust the model fluid chemistry for charge balance, initially modifying Na<sup>+</sup> and then Ca<sup>2+</sup> to accommodate Fe<sup>2+</sup> (Table 6). Iron is set at a concentration of 1 mmol/kg to saturate fluids with respect to minerals in the Fe-O-S system. Following Berndt et al. (1989), dissolved Si, Al and pH are controlled by coexistence of quartz, plagioclase ( $An_{60}$ ), and clinozoisite. The presence of these buffering mineral assemblages results in an in situ pH of 5.5-6.5 throughout the H2 - H2S activity region populated by hydrothermal vent fluids, similar to the measured and calculated pH of natural fluids (Ding et al., 2005).

At the typical vent fluid temperatures of 350 °C, calculated molybdenite-saturated Mo concentrations are 5 nmol/kg if H2 and H2S are buffered by Py-Po-Mag and 400 nmol/kg if buffered by Hem-Py-

Table 6 Initial fluid chemistry used in the model.

Model Input Parameteru					
Temperature	°C	350			
Cl <sup>-</sup>	mmol/kg	520			
Na <sup>+</sup>	mmol/kg	440			
Ca <sup>2+</sup>	mmol/kg	39			
Fe <sup>2+</sup>	mmol/kg	1			
SiO <sub>2</sub>	buffer	quartz			
H+	buffer	clinosoisite			
Al <sup>3+</sup>	buffer	An <sub>60</sub>			
Mo	buffer	molybdenite			
H <sub>2</sub> S	vary	-			
H <sub>2</sub>	vary				

Mag. Predicted Mo concentrations are 180 nmol/kg at the H<sub>2</sub> - H<sub>2</sub>S conditions of the 350 °C experiments. Notably, predicted Mo concentrations values are 4–5 times less than those measured in experimental fluids, suggesting that current theoretical models underpredict molybdenite solubility or that the experimental hydrothermal fluids are supersaturated with respect to molybdenite. Either way, vent fluids may be expected to contain higher concentrations of Mo than current theoretical models predict, especially if vent fluid Mo concentrations reflect effective equilibration with molybdenite at higher-than-venting temperatures, as has been suggested to explain the chemistry of MEF 2019–2020 time series vent fluids (Evans et al., 2023) (Fig. 12).

## 4.4. Modern and Archean flux estimates

Evidence from hydrothermal experiments, natural samples, and thermodynamic models all point to a high degree of temperature sensitivity in vent fluid Mo concentrations, which in turn implies that Mo concentrations in hydrothermal fluids are susceptible to Mo deposition at nearly all stages of vent fluid upflow. Thus, predicted vent fluid Mo concentrations are inherently uncertain owing to a lack of knowledge about vent fluid upflow pathways and the likelihood of site-specific variability. Moreover, the available thermodynamic models for Mo aqueous speciation and MoS2 solubility are still in a state of development and will need to be improved to accurately calculate Mo concentrations over the full range of chemical and physical conditions that may be experienced by deeply source hydrothermal fluids. Nevertheless, a synopsis of experimental, theoretical, and field sampling approaches suggests a fairly narrow range of likely vent fluid Mo concentrations useful for generating semi-quantitative "order-of-magnitude" estimates of Modern and Archean vent fluid Mo concentrations and fluxes.

For modern basalt-hosted vent fluids, we estimate vent fluid Mo concentrations of 30-1500 nmol/kg, which is 4 times the 350 °C model predictions for the Py-Po-Mag buffer and Hem-Py-Mag buffer, respectively, as is consistent with the difference between model and

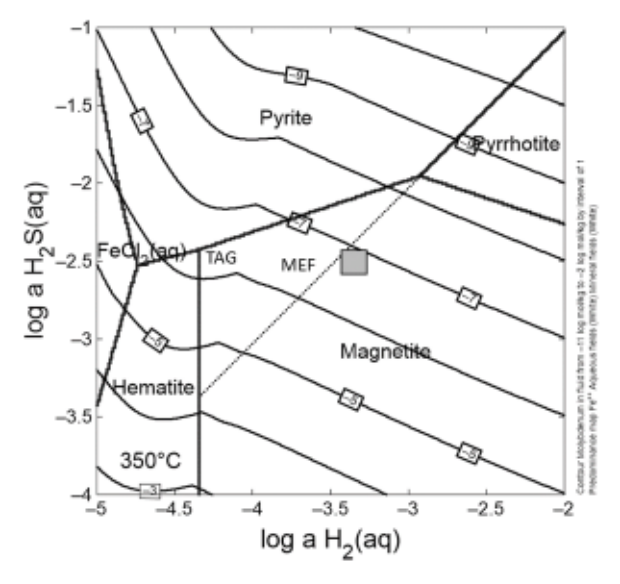


Fig. 12. Results of thermodynamic calculations of molybdenite solubility at 350 °C for varying H<sub>2</sub> and H<sub>2</sub>S activities. Contour maps of calculated molybdenite-saturated Mo concentrations are labeled in units of log<sub>10</sub>(mol/kg). Mineral stability fields in the Fe-O-S system and metastable extension of the pyrite-pyrrhotite tie line are shown to facilitate comparison with previous work (e.g., Klein et al., 2020). Fluid chemistry of the TAG hydrothermal mound (TAG), the Main Endeavour Field (MEF) 2019–2020 time series, and the experimental conditions (gray box) are also shown for reference. Predicted molybdenite solubility at these conditions is 100–1000 nmol/kg, in order-of-magnitude agreement with measured values. Figure was constructed using the Phase2 module in GWB.

experimental results. This concentration can be multiplied by an estimated modern day high-temperature mid-ocean ridge hydrothermal water flux of  $3\times 10^{12}$  kg/yr (Elderfield and Schultz, 1996) to achieve a modern seafloor hydrothermal Mo flux of  $9\times 10^4$ –4.5  $\times 10^6$  mol/yr. For comparison, the modern continental flux of Mo to the ocean is estimated at  $3.1\times 10^8$  mol/yr (Miller et al., 2011). Miller et al. (2011) estimate a modern continental Mo flux of  $3.1\times 10^8$  mol/yr and a modern seafloor hydrothermal Mo input of  $6.6\times 10^5$  mol/yr. This hydrothermal input is estimates using a hydrothermal water flux of  $3\times 10^{13}$  kg/yr, representative of both high- and low-temperature venting, and a hydrothermal fluid concentration of 22 nmol/kg. Our proposed estimates are at most 1.5% of the modern continental runoff flux, consistent with previous descriptions of the modern Mo geochemical cycle in which continental weathering and runoff constitutes the dominant source of Mo to the ocean

For Archean basalt-hosted vent fluids, we estimate that vent fluid Mo concentrations would have been roughly similar to modern vent fluid concentrations but consider that upper values may have been limited by the availability of Mo in oceanic crust derived from higher-degree mantle melting. For example, McCoy-West et al. (2019) propose that Archean seafloor derived from an estimated ~30% partial melt of mantle material and contained 155 ng/g Mo. Assuming a 1:1 fluid:rock ratio, this concentration is sufficient to support a maximum concentration of approximately 1600 nmol/kg Mo in hydrothermal fluids, which is greater than our upper estimate of 1500 nmol/kg for modern vent fluids. It has also been proposed that higher heat fluxes during the Archean resulted in more widespread hydrothermal activity. For example, Kamber (2010) estimate seafloor hydrothermal water fluxes of  $7.5 \times 10^{12}$  kg/yr at 2.4 Ga ago and  $1.5 \times 10^{13}$  kg/yr at 4.5 Ga ago based on scaling to oceanic crustal production rates and geochemical modeling of rare-earth element signatures and Sr and Nd isotopes in Archean hydrogenous sediments. Applying these estimates of hydrothermal fluid flux to our estimated of vent fluid Mo concentrations results in an estimated seafloor hydrothermal Mo flux of  $2 \times 10^5$ – $1 \times 10^7$  mol/yr 2.4 Ga ago and  $4 \times 10^5 - 2 \times 10^7$  mol/yr 4.5 Ga ago.

More significantly, the Archean atmosphere contained much less oxygen with estimated atmospheric  $O_2 = 10^{-6.9} - 10^{-6}$  the present atmospheric level (Catling and Zahnle, 2020; Johnson et al., 2021). Experimental studies indicate that oxidative weathering of pyrite and molybdenite both have a square root rate dependence on O2 partial pressure (Johnson et al., 2019). Hence, assuming that the availability of Mo in subaerial Archean crustal rocks was roughly the same as modern continental crust, it might be expected that Archean continental fluxes of Mo were  $10^{-3.5}$ – $10^{-3}$  modern day fluxes, or  $1.1 \times 10^{5}$ – $3.1 \times 10^{5}$  kg/ yr, which is roughly equivalent to our lower estimates for Archean hydrothermal fluxes. These estimates strongly suggest that seafloor hydrothermal vents were a significant and quite possibly the dominant source of Mo to the ocean throughout the Archean Eon, providing a baseline level of Mo that would have been at least locally sufficient to support the development and evolution of Mo-dependent enzymes. Moreover, vent fluid concentrations of Mo and Fe exceed those of Molimited and Fe-limited N2 fixation experiments (Mo = 100 nmol/kg Mo, Fe = 2400 nmol/kg, Zerkle et al., 2006). Thus, seafloor hydrothermal vents represent localized Mo-rich environments conducive to the emergence, evolution, and genetic retention of Mo-dependent enzymes. That vent fluid Mo predominantly enters the ocean as Fe- and Srich hydrothermal plume particles may be significant in light of the functional role of Mo-S- and Mo-Fe-S-containing cofactors in enzymatic chemistry.

#### 5. Conclusions

An investigation of experimental reaction fluids and solid run products from hydrothermal basalt alterations experiments combined with thermodynamic calculations and previous analyses of altered oceanic crust, seafloor hydrothermal fluids, and near-vent plume

particles leads to a new conceptual model for the behavior of Mo in basalt-hosted seafloor hydrothermal systems. Molybdenum, assumed to be hosted in volcanic glass and Fe-Ti oxide minerals in primary basalt is effectively leached by high-temperature subseafloor hydrothermal fluids and redeposited as molybdenite, as observed in Mo-enriched samples of altered oceanic crust from Pito Deep Rift. Comparison of reaction fluids from 350 C 500 hydrothermal basalt alteration experiments with thermodynamic predictions of Mo concentrations based on molybdenite solubility suggest that Mo concentrations in subsurface hydrothermal fluids are generally controlled by the solubility of molybdenite in the context of rock-derived buffering mineral assemblages that control major fluid chemical parameters including pH, H<sub>2</sub>S and H<sub>2</sub> as well as fluid temperature and salinity. A time series of nine 281 304 C seafloor vent fluids collected from Main Endeavour Field contains 29 220 nmol/kg Mo. These fluids are highly supersaturated with respect to molybdenite at venting conditions, suggesting both that vent fluid Mo concentrations reflect higher-temperature subsurface conditions and that vent fluid Mo concentrations are highly susceptible to processes that induce subsurface deposition. The MEF 2019 2020 time series exhibits two distinct decreases in Mo concentrations: one coincident with a subsurface intrusion of partially reacted seawater and a second coincident with a decrease in vent fluid temperature. Analyses of vent fluid particulate fractions reveal Mo:Cu ratios and concentrations resembling the hydrothermal endmember of near-vent sediment samples. This observation suggests: (1) that vent fluid Mo is readily incorporated into hydrothermal plume particles and, (2) that much of this vent fluid Mo source is advected out of the near-vent environment as suspended hydrothermal plume particles, as previous studies estimate that 2% of vent fluid Cu is deposited in the near-vent field.

Overall, these investigations demonstrate that seafloor hydrothermal vent fluids likely contain 10 1000 nmol/kg Mo and that this concentration can be entirely supported by underlying rocks, independent of seawater-derived Mo. Whether this concentration represents a net sink or source to the ocean depends much on seawater Mo concentrations. For the modern ocean containing 108 5 nmol/kg Mo, we estimate that seafloor hydrothermal vent fluids constitute a minor source of Mo, overshadowed by the much larger continental runoff flux and high seawater Mo concentrations. For Mo-poor Archean oceans, however, we estimate that seafloor hydrothermal vent fluids would have provided a significant and quite probably dominant source of Mo to the ocean delivered largely in the form of hydrothermal plume particles. Identification of this source and its likely form as solid metal-sulfide particles has important implications for theories concerning the evolution of Modependent enzymes, including nitrogenase and CO-dehydrogenase.

# Data availability

Data are included in Supplementary Materials. Additional raw data are available upon request to the authors.

# **Declaration of Competing Interest**

The authors declare that they have no known competing financial interests or personal relationships that could have appeared to influence the work reported in this paper.

## Acknowledgements

This study was funded by the NASA Astrobiology Program ICAR grant [80NSSC21K0592] Title: What life wants: Exploring the natural selection of elements to BK (PI), GNE, and WES, funded by the Metal Utilization and Selection across Eons (MUSE) Interdisciplinary Consortium for Astrobiology Research (ICAR) at the University of Wisconsin - Madison, sponsored by the National Aeronautics and Space Administration Science Mission Directorate (19-ICAR19\_2-0007). Additional funding was provided by the National Science Foundation Marine

Geology & Geophysics (MGG 1736679).

We especially thank Ariel Anbar for his intellectual energy and ongoing contributions to the MUSE ICAR. We also thank Aleisha Johnson, Chad Ostrander, and Amanda Garcia for participating in engaging and useful discussions on Mo geochemical cycling and Mo-dependent enzymes. We additionally thank Eva Stüecken, Dionysis Foustoukos, and two anonymous reviewers for their insightful comments and suggestions that contributed to the improvement of this publication.

Portions of this work were performed at GeoSoilEnviroCARS (The University of Chicago, Sector 13), Advanced Photon Source (APS), Argonne National Laboratory. GeoSoilEnviroCARS is supported by the National Science Foundation Earth Sciences (EAR 1634415). This research used resources of the Advanced Photon Source, a U.S. Department of Energy (DOE) Office of Science User Facility operated for the DOE Office of Science by Argonne National Laboratory under Contract No. DE-ACO2-06CH11357. We thank Matt Newville and Tony Lanzirotti at GeoSoilEnviroCARS for their hospitality and expertise.

We wish to thank Ocean Networks Canada including the affiliated vessel crews and ROV pilot teams for building and maintaining the NEPTUNE cabled observatory and providing support for seafloor sample collection. Partial funding towards the project was provided by Canadian Foundation for Innovation Project 30867.

## Appendix A. Supplementary material

Supplementary material to this article can be found online at htt ps://doi.org/10.1016/j.gca.2023.05.018.

#### References

- Anbar, A.D., Knoll, A.H., 2002. Proterozoic ocean chemistry and evolution: a bioinorganic bridge. Science (80-.) 297, 1137 1142.
- Awolayo, A.N., Tutolo, B.M., 2022. PyGeochemCalc: A Python package for geochemical thermodynamic calculations from ambient to deep Earth conditions. Chem. Geol. 606, 120984.
- Berndt, M.E., Seyfried, W.E., Janecky, D.R., 1989. Plagioclase and epidote buffering of cation ratios in mid-ocean ridge hydrothermal fluids: Experimental results in and near the supercritical region. Geochim. Cosmochim. Acta 53 (9), 2283 2300.
- Bethke, C.M., Yeakel, S., 2012. The Geochemist's Workbench (Version 9.0): Reaction Modeling Guide. Aqueous Solutions, LLC, Champaign, Ill.
- Boyd, E.S., Hamilton, T.L., Peters, J.W., 2011. An alternative path for the evolution of biological nitrogen fixation. Front. Microbiol. 2, 205.
- Burgess, B.K., Lowe, D.J., 1996. Mechanism of molybdenum nitrogenase. *Chem. Rev.* 96 (7), 2983–3012.
- Butterfield, D.A., Massoth, G.J., 1994. Geochemistry of north Cleft segment vent fluids: Temporal changes in chlorinity and their possible relation to recent volcanism. J. Geophys. Res. Solid Earth 99 (B3), 4951–4968.
- Canfield, D.E., 2005. The early history of atmospheric oxygen. Annu. Rev. Earth Planet. Sci 33 (1), 36.
- Cao, X., 1989. Solubility of Molybdenite and the Transport of Molybdenium in Hydrothermal Solutions. Iowa State University.
- Catling, D.C., Zahnle, K.J., 2020. The Archean atmosphere. Sci. Adv. 6 (9), eaax1420. Coogan, L.A., Attar, A., Mihaly, S.F., Jeffries, M., Pope, M., 2017. Near-vent chemical processes in a hydrothermal plume: Insights from an integrated study of the Endeavour segment. Geochem. Geophys. Geosys. 18 (4), 1641 1660.
- Danielson, L.R., Righter, K., Newville, M., Sutton, S., Choi, Y., Pando, K., 2011.
  Molybdenum valence in basaltic silicate melts: effects of temperature and pressure.
  42nd Lunar and planetary science conference (No. JSC-CN-22824).
- Delaney, J.R., Robigou, V., McDuff, R.E., Tivey, M.K., 1992. Geology of a vigorous hydrothermal system on the Endeavour Segment, Juan de Fuca Ridge. J. Geophys. Res. Solid Earth 97 (B13), 19663 19682.
- Diehl, A., Bach, W., 2020. MARHYS (MARine HYdrothermal Solutions) Database: A global compilation of marine hydrothermal vent fluid, end member, and seawater compositions. Geochem. Geophys. Geosyst. 21 (12), e2020GC009385.
- Ding, K., Seyfried, W.E., Zhang, Z., Tivey, M.K., Von Damm, K.L., Bradley, A.M., 2005. The *in situ* pH of hydrothermal fluids at mid-ocean ridges. Earth Planet. Sci. Lett. 237 (1–2), 167–174.
- Douville, E., Charlou, J.L., Oelkers, E.H., Bienvenu, P., Colon, C.J., Donval, J.P., Fouquet, Y., Prieur, D., Appriou, P., 2002. The Rainbow vent fluids (36 14 N, MAR): the influence of ultramafic rocks and phase separation on trace metal content in Mid-Atlantic Ridge hydrothermal fluids. Chem. Geol. 184 (1 2), 37 48.
- Elderfield, H., Schultz, A., 1996. Mid-ocean ridge hydrothermal fluxes and the chemical composition of the ocean. Annual Rev. Earth Planet. Sci. 24 (1), 191 224.
- Erickson, B.E., Helz, G.R., 2000. Molybdenum (VI) speciation in sulfidic waters: stability and lability of thiomolybdates. Geochim. Cosmochim. Acta 64 (7), 1149 1158.

- Evans, G.N., Seyfried Jr, W.E., Tan, C., 2023. Nutrient transition metals in a time series of hydrothermal vent fluids from Main Endeavour Field, Juan de Fuca Ridge, Pacific Ocean. Earth Planet. Sci. Lett. 602, 117943.
- Falkowski, P.G., Fenchel, T., Delong, E.F., 2008. The microbial engines that drive Earth s biogeochemical cycles. Science 320 (5879), 1034 1039.
- Findlay, A.J., Gartman, A., Shaw, T.J., Luther III, G.W., 2015. Trace metal concentration and partitioning in the first 1.5 m of hydrothermal vent plumes along the Mid-Atlantic Ridge: TAG, Snakepit, and Rainbow. Chem. Geol. 412, 117 131.
- Findlay, A.J., Estes, E.R., Gartman, A., Yücel, M., Kamyshny, A., Luther, G.W., 2019. Iron and sulfide nanoparticle formation and transport in nascent hydrothermal vent plumes. Nat. Commun. 10 (1), 1 7.
- Gale, A., Dalton, C.A., Langmuir, C.H., Su, Y., Schilling, J.G., 2013. The mean composition of ocean ridge basalts. Geochem. Geophys. Geosyst. 14, 489 518.
- Garcia, A.K., McShea, H., Kolaczkowski, B., Kaçar, B., 2020. Reconstructing the evolutionary history of nitrogenases: Evidence for ancestral molybdenum-cofactor utilization. Geobiology 18 (3), 394 411.
- Garcia, A.K., Kolaczkowski, B., Kaçar, B., 2022. Reconstruction of nitrogenase predecessors suggests origin from maturase-like proteins. Genome Bio. Evol. 14 (3), evac031.
- Gartman, A., Findlay, A.J., Luther III, G.W., 2014. Nanoparticulate pyrite and other nanoparticles are a widespread component of hydrothermal vent black smoker emissions. Chem. Geol. 366, 32 41.
- Grant, H.L., Hannington, M.D., Petersen, S., Frische, M., Fuchs, S.H., 2018. Constraints on the behavior of trace elements in the actively-forming TAG deposit, Mid-Atlantic Ridge, based on LA-ICP-MS analyses of pyrite. Chem. Geol. 498, 45–71.
- Greaney, A.T., Rudnick, R.L., Helz, R.T., Gaschnig, R.M., Piccoli, P.M., Ash, R.D., 2017.
  The behavior of chalcophile elements during magmatic differentiation as observed in Kilauea Iki lava lake, Hawaii. *Geochim. Cosmochim. Acta* 210, 71–96.
- Greaney, A.T., Rudnick, R.L., Gaschnig, R.M., Whalen, J.B., Luais, B., Clemens, J.D., 2018. Geochemistry of molybdenum in the continental crust. Geochim. Cosmochim. Acta 238, 36–54.
- Hannington, M.D., Galley, A.G., Herzig, P., Petersen, S., 1998. Comparison of the TAG mound and stockwork complex with Cyprus-type massive sulfide deposits. In: Proceedings of the Ocean Drilling Program: Scientific Results, Vol. 158. University, pp. 389 415.
- Heft, K., Gillis, K.M., Pollock, M.A., Karson, J.A., Klein, E.M., 2008. Constraints on the nature of axial hydrothermal systems from the sheeted dike complex exposed at Pito Deep. Geochem. Geophys. Geosyst. 9 (5).
- Hekinian, R., Bideau, D., Francheteau, J., Cheminee, J.L., Armijo, R., Lonsdale, P., Blum, N., 1993. Petrology of the East Pacific Rise crust and upper mantle exposed in Hess Deep (eastern equatorial Pacific). J. Geophys. Res.: Solid Earth 98 (B5), 8069-8094.
- Helz, G.R., 2021. Dissolved molybdenum asymptotes in sulfidic waters. Chem. Geol. 289, 1–11.
- Ho, P., Lee, J.M., Heller, M.I., Lam, P.J., Shiller, A.M., 2018. The distribution of dissolved and particulate Mo and V along the US GEOTRACES East Pacific Zonal Transect (GP16): The roles of oxides and biogenic particles in their distributions in the oxygen deficient zone and the hydrothermal plume. Mar. Chem. 201, 242–255.
- Holland, H.D., 2002. Volcanic gases, black smokers, and the Great Oxidation Event. Geochim. Cosmochim. Acta 66 (21), 3811 3826.
- Hrischeva, E., Scott, S.D., 2007. Geochemistry and morphology of metalliferous sediments and oxyhydroxides from the Endeavour segment, Juan de Fuca Ridge. Geochim. Cosmochim. Acta 71 (14), 3476–3497.
- Huston, D.L., Brauhart, C.W., Drieberg, S.L., Davidson, G.J., Groves, D.I., 2001. Metal leaching and inorganic sulfate reduction in volcanic-hosted massive sulfide mineral systems: Evidence from the paleo-Archean Panorama district, Western Australia. *Geology* 29 (8), 687–690.
- James, R.H., Elderfield, H., Palmer, M.R., 1995. The chemistry of hydrothermal fluids from the Broken Spur site, 29 N Mid-Atlantic Ridge. Geochim. Cosmochim. Acta 59 (4), 651–659.
- Jochum, K.P., Weis, U., Schwager, B., Stoll, B., Wilson, S.A., Haug, G.H., Andreae, M.O., Enzweiler, J., 2016. Reference values following ISO guidelines for frequently requested rock reference materials. Geostand. Geoanal. Res. 40 (3), 333 350.
- Joerger, R.D., Bishop, P.E., Evans, H.J., 1988. Bacterial alternative nitrogen fixation systems. CRC Crit. Rev. Microbiol. 16 (1), 1 14.
- Johnson, A.C., Romaniello, S.J., Reinhard, C.T., Gregory, D.D., Garcia-Robledo, E., Revsbech, N.P., Canfield, D.E., Lyons, T.W., Anbar, A.D., 2019. Experimental determination of pyrite and molybdenite oxidation kinetics at nanomolar oxygen concentrations. Geochim. Cosmochim. Acta 249, 160 172.
- Johnson, A.C., Ostrander, C.M., Romaniello, S.J., Reinhard, C.T., Greaney, A.T., Lyons, T. W., Anbar, A.D., 2021. Reconciling evidence of oxidative weathering and atmospheric anoxia on Archean Earth. Sci. Adv. 7 (40), eabj0108.
- Kamber, B.S., 2010. Archean mafic ultramafic volcanic landmasses and their effect on ocean atmosphere chemistry. Chem. Geol. 274 (1 2), 19 28.
- Kelley, D.S., Delaney, J.R., Juniper, S.K., 2014. Establishing a new era of submarine volcanic observatories: Cabling Axial Seamount and the Endeavour Segment of the Juan de Fuca Ridge. Mar. Geol. 352, 426–450.
- Kendall, B., Dahl, T.W., Anbar, A.D., 2017. The stable isotope geochemistry of molybdenum. Rev. Mineral. Geochem. 82 (1), 683 732.
- Klein, F., Tarnas, J.D., Bach, W., 2020. Abiotic sources of molecular hydrogen on Earth. Elements 16 (1), 19 24.
- Klose, L., Kleint, C., Bach, W., Diehl, A., Wilckens, F., Peters, C., Strauss, H., Haase, K., Koschinsky, A., 2022. Hydrothermal activity and associated subsurface processes at Niuatahi rear-arc volcano, North East Lau Basin, SW Pacific: Implications from trace elements and stable isotope systematics in vent fluids. Geochim. Cosmochim. Acta 332, 103 123.

- Liu, W., Etschmann, B., Mei, Y., Guan, Q., Testemale, D., Brugger, J., 2020. The role of sulfur in molybdenum transport in hydrothermal fluids: Insight from in situ synchrotron XAS experiments and molecular dynamics simulations. Geochim. Cosmochim. Acta 290, 162 179.
- Lyons, T.W., Reinhard, C.T., Planavsky, N.J., 2014. The rise of oxygen in Earth's early ocean and atmosphere. Nature 506 (7488), 307–315.
- Maia, L.B., Moura, I., Moura, J.J., 2016. Molybdenum and tungsten-containing enzymes: an overview.
- McCoy-West, A.J., Chowdhury, P., Burton, K.W., Sossi, P., Nowell, G.M., Fitton, J.G., Kerr, A.C., Cawood, P.A., Williams, H.M., 2019. Extensive crustal extraction in Earth's early history inferred from molybdenum isotopes. Nat. Geosci. 12 (11), 946–951.
- Metz, S., Trefry, J.H., 2000. Chemical and mineralogical influences on concentrations of trace metals in hydrothermal fluids. Geochim. Cosmochim. Acta 64 (13), 2267 2279.
- Miller, R.W., Eady, R.R., 1988. Molybdenum and vanadium nitrogenases of Azotobacter chroococcum. Low temperature favours N2 reduction by vanadium nitrogenase. Biochem. J. 256 (2), 429–432.
- Miller, C.A., Peucker-Ehrenbrink, B., Walker, B.D., Marcantonio, F., 2011. Re-assessing the surface cycling of molybdenum and rhenium. Geochim. Cosmochim. Acta 75 (22), 7146–7179.
- Minubayeva, Z., Seward, T.M., 2010. Molybdic acid ionisation under hydrothermal conditions to 300 C. Geochim. Cosmochim. Acta 74 (15), 4365–4374.
- Morel, F.M., Price, N.M., 2003. The biogeochemical cycles of trace metals in the oceans. Science 300 (5621), 944 947.
- Newville, M., 2013, Larch: an analysis package for XAFS and related spectroscopies. In: Journal of Physics: Conference Series (Vol. 430, No. 1, p. 012007). IOP Publishing.
- O Neill, H.S.C., Eggins, S.M., 2002. The effect of melt composition on trace element partitioning: an experimental investigation of the activity coefficients of FeO, NiO, CoO, MoO<sub>2</sub> and MoO<sub>3</sub> in silicate melts. Chem. Geol. 186 (1 2), 151 181.
- Parsons, C., Stüeken, E.E., Rosen, C.J., Mateos, K., Anderson, R.E., 2021. Radiation of nitrogen-metabolizing enzymes across the tree of life tracks environmental transitions in Earth history. Geobiology 19 (1), 18–34.
- Perfit, M.R., Cann, J.R., Fornari, D.J., Engels, J., Smith, D.K., Ian Ridley, W., Edwards, M. H., 2003. Interaction of sea water and lava during submarine eruptions at mid-ocean ridges. Nature 426 (6962), 62 65.
- Pester, N.J., Rough, M., Ding, K., Seyfried, W.E., 2011. A new Fe/Mn geothermometer for hydrothermal systems: Implications for high-salinity fluids at 13 N on the East Pacific Rise, Geochim, Cosmochim, Acta 75 (24), 7881 7892.
- Petersen, S., Herzig, P.M., Kuhn, T., Franz, L., Hannington, M.D., Monecke, T., Gemmell, J.B., 2005. Shallow drilling of seafloor hydrothermal systems using the BGS Rockdrill: Conical Seamount (New Ireland fore-arc) and PACMANUS (eastern Manus basin), Papua New Guinea. Mar. Geores. Geotech. 23 (3), 175 193.
- Pokrovski, G.S., Borisova, A.Y., Harrichoury, J.-C., 2008. The effect of sulfur on vapor liquid fractionation of metals in hydrothermal systems. Earth Planet. Sci. Lett. 266 (3), 345–362.
- Raymond, J., Siefert, J.L., Staples, C.R., Blankenship, R.E., 2004. The natural history of nitrogen fixation. Mol. Biol. Evol. 21 (3), 541–554.
- Robie, R.A., Hemingway, B.S., 1995. Thermodynamic properties of minerals and related substances at 298.15 K and 1 bar (105 Pascals) pressure and at higher temperatures (No. 2131). US Government Printing Office.
- Sanchez-Baracaldo, P., Ridgwell, A., Raven, J.A., 2014. A neoproterozoic transition in the marine nitrogen cycle. Curr. Biol. 24 (6), 652–657.
   Schmidt, K., Koschinsky, A., Garbe-Schonberg, D., de Carvalho, L.M., Seifert, R., 2007.
- Schmidt, K., Koschinsky, A., Garbe-Schonberg, D., de Carvalho, L.M., Seifert, R., 2007. Geochemistry of hydrothermal fluids from the ultramafic-hosted Logatchev hydrothermal field, 15 N on the Mid-Atlantic Ridge: Temporal and spatial investigation. Chem. Geol. 242 (1 2), 1 21.
- Schmidt, K., Garbe-Schonberg, D., Koschinsky, A., Strauss, H., Jost, C.L., Klevenz, V., Koniger, P., 2011. Fluid elemental and stable isotope composition of the Nibelungen hydrothermal field (8 18 S, Mid-Atlantic Ridge): constraints on fluid rock interaction in heterogeneous lithosphere. Chem. Geol. 280 (1 2), 1 18.
- Schoepp-Cothenet, B., Van Lis, R., Philippot, P., Magalon, A., Russell, M.J., Nitschke, W., 2012. The ineluctable requirement for the trans-iron elements molybdenum and/or tungsten in the origin of life. Sci. Rep. 2 (1), 1 5.
- Seewald, J.S., Seyfried, W.E., 1990. The effect of temperature on metal mobility in subseafloor hydrothermal systems: constraints from basalt alteration experiments. Earth Planet. Sci. Lett. 101 (2 4), 388 403.
- Seyfried, W.E., Bischoff, J.L., 1981. Experimental seawater-basalt interaction at 300 C, 500 bars, chemical exchange, secondary mineral formation and implications for the transport of heavy metals. Geochim. Cosmochim. Acta 45 (2), 135 147.
- Seyfried, W.E., Ding, K., 1993. The effect of redox on the relative solubilities of copper and iron in Cl-bearing aqueous fluids at elevated temperatures and pressures: an experimental study with application to subseafloor hydrothermal systems. Geochim. Cosmochim. Acta 57 (9), 1905–1917.
- Seyfried, W.E., Ding, K., 1995. Phase equilibria in subseafloor hydrothermal systems: A review of the role of redox, temperature, pH and dissolved Cl on the chemistry of hot spring fluids at mid-ocean ridges. Washington DC Am. Geophys. Union Geophys. Monogr. Ser. 91, 248 272.
- Seyfried, W.E., Janecky, D.R., 1985. Heavy metal and sulfur transport during subcritical and supercritical hydrothermal alteration of basalt: Influence of fluid pressure and basalt composition and crystallinity. Geochim. Cosmochim. Acta 49 (12), 2545–2560.
- Seyfried, W.E., Janecky, D.R., Berndt, M.E., Ulmer, G.C., Barnes, H.L., 1987. Rocking autoclaves for hydrothermal experiments II. The flexible reaction-cell system. Hydrothermal Exp. Tech. 23.

- Seyfried, W.E., Seewald, J.S., Berndt, M.E., Ding, K., Foustoukos, D.I., 2003. Chemistry of hydrothermal vent fluids from the Main Endeavour Field, northern Juan de Fuca Ridge: Geochemical controls in the aftermath of June 1999 seismic events. J. Geophys. Res. Solid Earth 108 (B9).
- Seyfried, W.E., Tan, C., Wang, X., Wu, S., Evans, G.N., Coogan, L.A., Mihaly, S.F., Lilley, M.D., 2022. Time series of hydrothermal vent fluid chemistry at Main Endeavour Field, Juan de Fuca Ridge: Remote sampling using the NEPTUNE cabled observatory. Deep Sea Res. Part I: Oceanogr. Res. Pap. 103809.
- Shang, L., Williams-Jones, A.E., Wang, X., Timofeev, A., Hu, R., Bi, X., 2020. An experimental study of the solubility and speciation of MoO3 (s) in hydrothermal fluids at temperatures up to 350 C. Econ. Geol. 115 (3), 661 669.
- Sheng, Y., Baars, O., Guo, D., Whitham, J., Srivastava, S., Dong, H., 2023. Mineral-Bound Trace Metals as Cofactors for Anaerobic Biological Nitrogen Fixation. Environmental Sci. Technol. 57 (18), 7206–7216.
- Shock, E.L., Helgeson, H.C., 1988. Calculation of the thermodynamic and transport properties of aqueous species at high pressures and temperatures: Correlation algorithms for ionic species and equation of state predictions to 5 kb and 1000 C. Geochim. Cosmochim. Acta 52 (8), 2009 2036.
- Shock, E.L., Helgeson, H.C., 1990. Calculation of the thermodynamic and transport properties of aqueous species at high pressures and temperatures: Standard partial molal properties of organic species. Geochim. Cosmochim. Acta 54 (4), 915–945.
- Shock, E.L., Helgeson, H.C., Sverjensky, D.A., 1989. Calculation of the thermodynamic and transport properties of aqueous species at high pressures and temperatures: Standard partial molal properties of inorganic neutral species. Geochim. Cosmochim. Acta 53 (9), 2157–2183.
- Shock, E.L., Sassani, D.C., Willis, M., Sverjensky, D.A., 1997. Inorganic species in geologic fluids: correlations among standard molal thermodynamic properties of aqueous ions and hydroxide complexes. Geochim. Cosmochim. Acta 61 (5), 907, 950
- Shvarov, Y.V., 2008. HCh: New potentialities for the thermodynamic simulation of geochemical systems offered by Windows. Geochem. Int. 46 (8), 834.
- Sillitoe, R.H., 2010. Porphyry copper systems. Econ. Geol. 105 (1), 3 41.
- Stüeken, E.E., Buick, R., Guy, B.M., Koehler, M.C., 2015. Isotopic evidence for biological nitrogen fixation by molybdenum-nitrogenase from 3.2 Gyr. Nature 520 (7549), 666–669.
- Tanger, J.C., Helgeson, H.C., 1988. Calculation of the thermodynamic and transport properties of aqueous species at high pressures and temperatures; revised equations of state for the standard partial molal properties of ions and electrolytes. Am. J. Sci. 288 (1), 19 98.

- Tivey, M.K., Humphris, S.E., Thompson, G., Hannington, M.D., Rona, P.A., 1995.

  Deducing patterns of fluid flow and mixing within the TAG active hydrothermal mound using mineralogical and geochemical data. J. Geophys. Res. Solid Earth 100 (B7), 12527 12555.
- Trefry, J.H., Butterfield, D.B., Metz, S., Massoth, G.J., Trocine, R.P., Feely, R.A., 1994.
  Trace metals in hydrothermal solutions from Cleft segment on the southern Juan de Fuca Ridge. J. Geophys. Res. Solid Earth 99 (B3), 4925–4935.
- Von Damm, K.L., Edmond, J.M., Grant, B., Measures, C.I., Walden, B., Weiss, R.F., 1985. Chemistry of submarine hydrothermal solutions at 21 N, East Pacific Rise. *Geochim. Cosmochim. Acta* 49 (11), 2197 2220.
- Weiss, M.C., Sousa, F.L., Mrnjavac, N., Neukirchen, S., Roettger, M., Nelson-Sathi, S., Martin, W.F., 2016. The physiology and habitat of the last universal common ancestor. Nat. Microbiol. 1 (9), 1 8.
- Wheat, C.G., Mottl, M.J., Rudnicki, M., 2002. Trace element and REE composition of a low-temperature ridge-flank hydrothermal spring. Geochim. Cosmochim. Acta 66 (21), 3693–3705.
- Wheat, C.G., Fisher, A.T., McManus, J., Hulme, S.M., Orcutt, B.N., 2017. Cool seafloor hydrothermal springs reveal global geochemical fluxes. Earth Planet. Sci. Lett. 476, 179, 188.
- Wille, M., Nebel, O., Van Kranendonk, M.J., Schoenberg, R., Kleinhanns, I.C., Ellwood, M.J., 2013. Mo Cr isotope evidence for a reducing Archean atmosphere in 3.46 2.76 Ga ago black shales from the Pilbara, Western Australia. Chem. Geol. 340, 68 76
- Wood, S.A., Crerar, D.A., Borcsik, M.P., 1987. Solubility of the assemblage pyrite-pyrrhotite-magnetite-sphalerite-galena-gold-stibnite-bismuthinite-argen-tite-molybdenite in H  $_2$  O-NaCl-CO  $_2$  solutions from 200  $\,$  C to 350  $\,$  C. Econ. Geol. 82 (7), 1864 1887.
- Xing, Y., Scheuermann, P., Seyfried Jr, W.E., 2021. Experimental study on Fe solubility in vapor-rich hydrothermal fluids at 400 500 C, 215 510 bar: Implication for Fe mobility in seafloor vent systems. Geochim. Cosmochim. Acta 314, 209 222.
- Xing, Y., Brugger, J., Scheuermann, P., Tan, C., Ji, S., Seyfried, W.E., 2022. An experimental and thermodynamic study of sphalerite solubility in chloride-bearing fluids at 300 450 C, 500 bar: implications for zinc transport in seafloor hydrothermal systems. Geochim. Cosmochim. Acta 330, 131 147.
- Zerkle, A.L., House, C.H., Cox, R.P., Canfield, D.E., 2006. Metal limitation of cyanobacterial N<sub>2</sub> fixation and implications for the Precambrian nitrogen cycle. Geobiol. 4 (4), 285–297.
- Zhu, T., 2016. Tracing on-axis diffuse fluids by chalcophile elements distribution in upper oceanic crust at Pito Deep, East Pacific Rise. University of Victoria.